CHALMERS
UNIVERSITY OF TECHNOLOGY

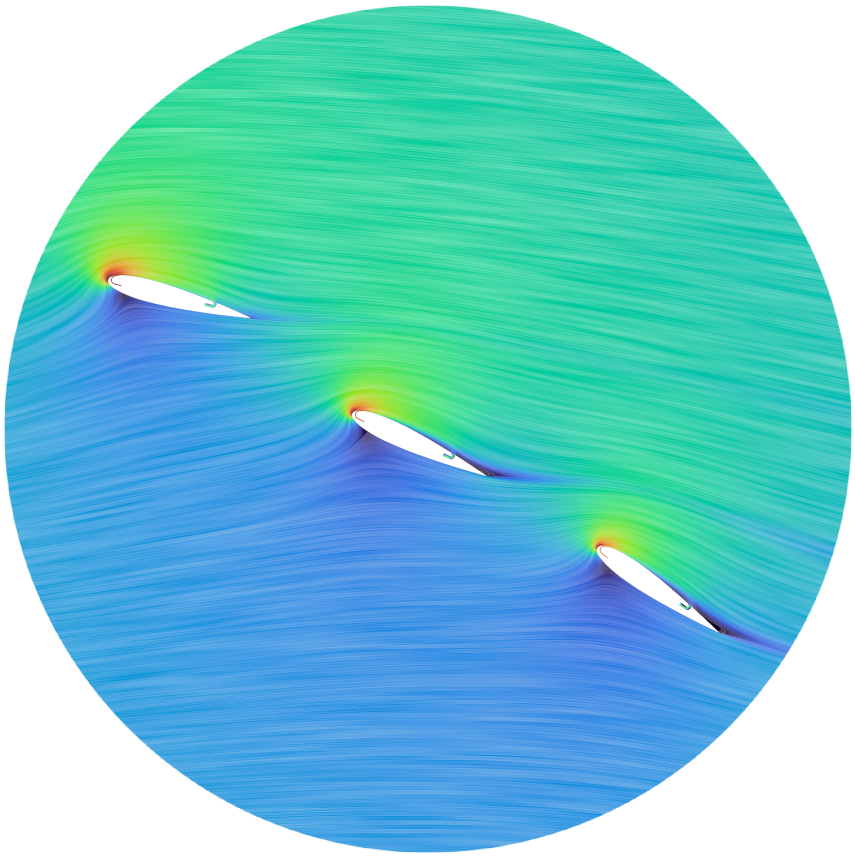

Aerodynamic Study of Multiple Wingsails with Co-Flow Jet Active Flow Control

Master's thesis in Applied Mechanics

PETTER ENGSTRÖM

DEPARTMENT OF MECHANICS AND MARITIME SCIENCES
CHALMERS UNIVERSITY OF TECHNOLOGY
Gothenburg, Sweden 2026
www.chalmers.se

Master's thesis 2026

Aerodynamic Study of Multiple Wingsails with Co-Flow Jet Active Flow Control

PETTER ENGSTRÖM

CHALMERS
UNIVERSITY OF TECHNOLOGY

Department of Mechanics and Maritime Sciences
Division of Marine Technology
Chalmers University of Technology
Gothenburg, Sweden 2026

Aerodynamic Study of Multiple Wingsails with Co-Flow Jet Active Flow Control
PETTER ENGSTRÖM

Supervisor: Kewei Xu, Mechanical Engineering, The University of Maine
Examiner: Rickard Bensow, Department of Mechanics and Maritime Sciences, Chalmers University of Technology

Master's Thesis 2026
Department of Mechanics and Maritime Sciences
Division of Marine Technology
Chalmers University of Technology
SE-412 96 Gothenburg
Telephone +46 31 772 1000

Acknowledgements, dedications, and similar personal statements in this thesis, reflect the author's own views.

Cover: Velocity streamlines of wingsails with co-flow jet active flow control in a three-sail configuration.

Printed by Chalmers Reproservice
Gothenburg, Sweden 2026

Aerodynamic Study of Multiple Wingsails with Co-Flow Jet Active Flow Control
PETTER ENGSTRÖM
Department of Mechanics and Maritime Sciences
Chalmers University of Technology

Abstract

Wingsails can be used as a means of reducing fuel consumption for maritime vessels. To improve on their performance there are different methods available, one of which is flow control. This thesis investigates how the co-flow jet (CFJ) active flow control (AFC) technology can improve the aerodynamic performance of a wingsail based on a NACA 0015 airfoil. The objective is to enhance thrust with minimal energy expenditure, thereby improving the net power savings of the wingsail. The study was performed using two-dimensional CFD simulations with the Unsteady Reynolds-averaged Navier–Stokes (URANS) equations and the k-ω Shear Stress Transport (SST) turbulence model. The baseline airfoil was modified to accommodate the CFJ requirements, which include injection and suction slots. A parametric study was performed on the resulting airfoil to establish an appropriate jet momentum coefficient (C_μ), together with the size and location of the slots. To make a direct comparison between a single CFJ and a baseline wingsail, a one-sail configuration was studied. Results demonstrate a substantial increase in thrust and net power savings for the CFJ wingsail. To study flow interactions between multiple wingsails, a three-sail configuration was studied, mimicking a vessel equipped with three wingsails. The study reveals that the wingsails are greatly affected by the apparent wind angle, with substantial flow interactions between the sails. In all tested conditions, the results demonstrate a significant improvement in propulsive performance. The findings also highlight the importance of a C_μ distribution strategy, together with individual adjustment of the angle of attack (AoA) of each wingsail. Overall, the CFJ technology applied to a wingsail is highly effective in preventing flow separation and improving performance over a wide range of operating conditions.

Keywords: co-flow jet, active flow control, wingsails, sail interactions, sustainable maritime transportation, wind-assisted propulsion system.

Acknowledgements

I would like to express my sincere gratitude to my supervisor, Kewei Xu, who through his mentorship has been fully supportive throughout this thesis. He has inspired and motivated me, ultimately leading to the publication of two papers based on this research in the AIAA SciTech conference proceedings [1, 2]. I am also grateful to Rickard Bensow for the opportunity to carry out my master's thesis at Chalmers University of Technology, as well as for their feedback. The motivational support and structural advice from Rasmus Lind have been indispensable.

Petter Engström, Gothenburg, June 2026

Nomenclature

AFC	Active Flow Control
AoA	Angle of Attack
AWA	Apparent Wind Angle
AWS	Apparent Wind Speed
CFJ	Co-Flow Jet
LE	Leading Edge
$NACA$	National Advisory Committee for Aeronautics
$RANS$	Reynolds-averaged Navier–Stokes
TE	Trailing Edge
TWS	True Wind Speed
$ZNMF$	Zero-Net Mass Flux
C	Chord length
$\%C$	Percent of chord length
C_D	Drag coefficient
C_L	Lift coefficient
C_p	Pressure coefficient
C_μ	Jet momentum coefficient
H_t	Total enthalpy
(L/D)	Aerodynamic efficiency
$(L/D)_c$	Aerodynamic efficiency corrected for CFJ
$\dot{m}$	Mass flow rate
P	Power consumption
P_c	Power coefficient
Ptr	Total pressure ratio
Re	Reynolds number
S	Planform area of the airfoil
T_t	Total temperature
U_∞	Freestream velocity

V_j	Mass-averaged velocity of the jet
α	Angle of attack
γ	Specific heat ratio
η	Efficiency of the micro-compressor
ρ_∞	Freestream density
$_c$	Subscript, corrected
$_j$	Subscript, jet

Contents

List of Figures

List of Tables

1
Introduction

This chapter introduces the background of the thesis. It starts with the importance of reducing the fuel consumption in the marine sector and explains different methods for doing so. The primary focus is on wingsails, the main theme of the thesis, and different flow control methods to improve their performance. Lastly, the aim and methodology are presented.

1.1 Background

Maritime transport handles 80% of all goods transported around the world and is responsible for 3% of the global greenhouse gas emissions. Although the amount of greenhouse gas per unit of transport work is relatively low, it is important to take action to prevent further increases in emissions. There is a constantly growing number of ships in the world. In January 2023, there were 105,493 ships in the world fleet with a gross tonnage of 100 tons and above. This fleet grew by 3.2% in 2022, and has grown steadily since the 1990s. The fleet is also aging, with an average age of 22.2 years as of 2023. Decarbonizing ships through the use of carbon-neutral fuels by 2050 is estimated to require a yearly investment of between $28 and $90 billion, potentially increasing annual fuel costs by 70% to 100% [3]. Therefore, reducing fuel consumption is of great importance. There are several ways to reduce the energy consumption of a ship. From a resistance mitigation perspective, there are air lubrication systems that reduce the hull friction on wetted surfaces. From a propulsion enhancement perspective, energy can be extracted from the wind to generate thrust. Popular wind propulsion technologies include rotor sails [4–6] based on the Magnus effect, kites [7–9], and wingsails [10–14]. Unlike conventional yacht sails, wingsails are rigid airfoil-shaped structures with higher aerodynamic efficiency and can be automated and retrofitted to existing ships. Oceanbird is one company that is currently developing such a system using multiple wingsails in a two-element setup. Their system uses a NACA 0025 as the main element and a NACA 0015 as an actuated flap [15]. Two of the aerodynamic challenges with wingsails are the interaction effects between the sails and the limiting angle of attack due to stall. These issues can be mitigated with the help of active flow control (AFC). The co-flow jet (CFJ) active flow control method, developed by Zha et al. [16] has previously been studied in an aircraft context [17–21]. This thesis investigates the CFJ method in a marine context.

1.1.1 Fuel reduction methods

There are multiple ways to reduce the fuel consumption of a ship, some of which are briefly described in this section.

Route planning

Optimized voyage planning can be split into two parts. Vessel-based optimization adjusts the route according to the vessels characteristics, such as ship speed, engine rotational speed, draft, trim and seekeeping behavior. Environmental-based optimization takes into account wind speed and direction, wave height, frequency and direction, and the currents [22].

Ship design

Fuel consumption can be reduced through various aspects of ship design. Regarding the hull, four common areas exist to improve its design. Hull form optimization uses techniques such as uncertainty analysis, operational research, and machine learning to minimize water resistance while still meeting cargo capacity, machinery, and accommodation requirements. Hull structure weight is reduced by optimizing the framework and using lighter materials. Hull cleaning prevents biofouling, the buildup of marine organisms on the hull that increases water resistance. Lastly, hull lubrication injects a layer of air bubbles along the bottom of the hull to reduce frictional resistance between the hull and water [23]. In terms of propulsion, diesel engines are the most common propulsion system. They are under constant development to improve their efficiency. Other ways of reducing their fuel consumption and emissions include hybrid electric systems using fuel cells or batteries, alternative fuels such as liquefied natural gas (LNG), or wind-assisted propulsion [24].

Wind-assisted propulsion

There are several ways to harness wind energy to assist ship propulsion. In addition to the traditional yacht sail, there are several more modern alternatives. Rotor sails, also referred to as Flettner rotors, are large vertical cylinders that utilize the Magnus effect to generate thrust [4–6]. Kites harvest wind power by being tethered to the bow of the ship, allowing the kites to capture wind energy at higher altitudes via control lines that can be automated [7–9]. Another alternative is the wingsail. They are airfoil-shaped rigid structures similar to an aircraft wing. Rather than being mounted horizontally to generate lift, wingsails are oriented vertically to generate thrust. This thrust is derived from a combination of lift and drag forces. Compared to traditional yacht sails, wingsails offer a higher aerodynamic efficiency and do not require running rigging.

1.1.2 Lift enhancement for wingsails

An airfoil can only increase its lift by increasing its AoA until it stalls. When it reaches its critical AoA flow separation occurs, reducing its performance. To overcome this issue different flow control methods can be utilized to delay transition or prevent separation, and therefore improve performance and extend the usable AoA range. Flow control can be divided into two categories, passive control and active control.

1.1.2.1 Passive flow control

Passive flow control requires no power or control system and manipulates the flow through geometrical features such as vortex generators, slats, and flaps. Vortex generators have the shape of small aspect ratio airfoils. By creating vortices they mix a high momentum flow

into the near-wall flow to increase the boundary layers resistance to separate. A drawback is that they introduce parasitic drag which also reduces the performance in conditions when they are not needed. Flaps and slats are additional aerodynamic surfaces mounted at the leading and trailing edges, usually integrated into the airfoil design. Besides being able to change the chord and camber of the airfoil, they direct high energy air through the slots they create onto the aerodynamic surfaces [25].

1.1.2.2 Active flow control

Active flow control methods require an external power source to function and need a control system. A benefit over the passive systems is that they can be adjusted or disabled depending on the what the conditions demand. A few different methods will be discussed in this section.

Plasma actuator

Plasma actuators are flow control devices that manipulate the boundary layer with the help of electrohydrodynamic (EHD) forces. By introducing a strong electric field, plasma is created through a process called ionization, producing particles with negative and positive charge. These ions move under the influence of the electric field and adds momentum to the airflow. Several types of plasma actuators exist, one of the most common for flow control is the dielectric barrier discharge (DBD) variant. It consists of two electrodes, one exposed and one embedded with a dielectric layer in between, as illustrated in Fig. 1.1. The electrodes are placed on the suction side near the leading edge of an airfoil. At activation a wall jet forms along the surface, energizing the boundary layer. Advantages of plasma actuators include their lack of moving parts, fast response time and low power consumption [26, 27].

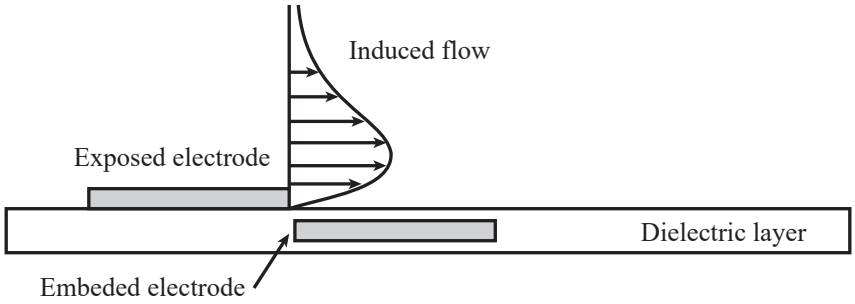

Figure 1.1: Schematics for a DBD plasma actuator.

Co-flow jet

The flow control method investigated in this thesis is the co-flow jet (CFJ) technique. It adds an injection slot close to the leading edge of the airfoil together with a suction slot close to the trailing edge, illustrated in Fig. 1.2. A jet is injected tangentially to the airfoil surface from the injection slot. An equal mass flow is withdrawn through the suction slot to achieve zero-net-mass-flux (ZNMF). The injected jet and the main flow interact, creating a turbulent shear layer which results in strong turbulent momentum diffusion and mixing. This enables the main flow to overcome the adverse pressure gradient created at high AoA and attaches the flow to the surface [28]. As a ZNMF system, the CFJ method does not introduce additional mass into the flow, instead it recirculates the same

air. The energy expenditure is only for driving the micro-compressor required to maintain the pressure difference between the two slots.

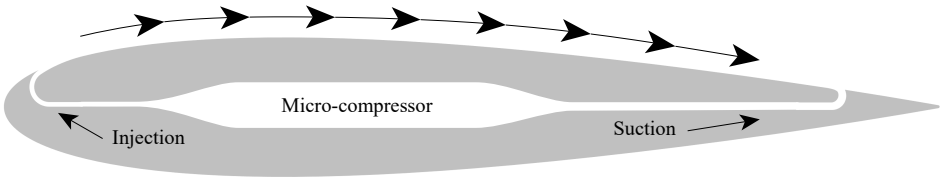

Figure 1.2: Schematic of a CFJ airfoil.

1.2 Aim

The aim of this thesis is to develop a fundamental understanding of how the co-flow jet affects the airflow around a NACA 0015 airfoil. This includes investigating how the intensity of the jet affects its aerodynamic properties and how the injection and suction slot locations and sizes affect the different performance parameters. Furthermore, a secondary objective is to study the aerodynamic interactions within a three-sail configuration, and whether there is any difference in behavior between a baseline airfoil and one equipped with CFJ.

1.3 Methodology

The thesis starts with creating a baseline NACA 0015 setup in the simulation software, which is used for validation and as a base for the following simulations. The next step is to modify the baseline airfoil design with CFJ ducts and to update the simulation setup to the changes required by the CFJ implementation. Subsequently, a parametric study is conducted to find an optimal configuration for the jet momentum coefficient and the design of the slots. This configuration is then adopted for a one-sail case where both the baseline and CFJ airfoils will be compared to each other. A three-sail configuration will also be studied to investigate how CFJ affects the flow interaction between the sails. These steps are illustrated in Fig. 1.3.

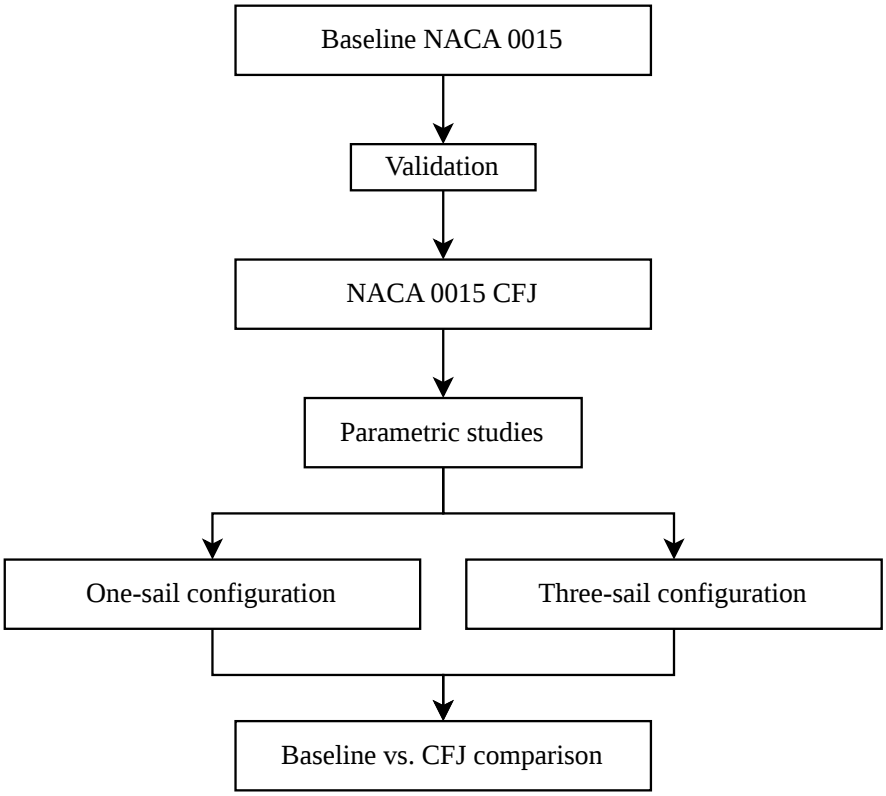

Figure 1.3: Methodology flow diagram.

1.4 Delimitations

Each of the five parametric studies is evaluated across a range of AoA, requiring a large number of simulations. The three-sail configuration further increases the computational demand. To reduce computational costs, all simulations are conducted in 2D using RANS. The simulations are additionally limited to only the wingsails themselves, with neither the hull nor the superstructure taken into consideration.

2
Theory

This chapter presents the fundamental theories and equations of fluid dynamics, the turbulence model, and the solver used in the simulations. It also introduces sailing related terms and physics. Lastly, the basic principles of flow control are explained, and the additional equations required for CFJ are presented.

2.1 Governing equations

The governing equations in fluid dynamics are a set of equations that describe the behavior of the motion of a fluid and how its properties change in space and time. Their main purpose is to enforce the conservation laws of physics.

Conservation of mass

The continuity equation represents the conservation of mass. It states that the rate of increase of mass in a fluid element equals the net flow of mass into the element, given by,

$$\frac{\partial \rho}{\partial t} + \rho \frac{\partial v_i}{\partial x_i} = 0, \tag{2.1}$$

where ρ is the density, v_i the velocity in the x direction, and t the time.

Conservation of momentum

The momentum equation is derived from Newton's second law of motion applied to a fluid element. It states that the rate of change of momentum equals the sum of all forces acting on the element, given by,

$$\rho \frac{\partial v_i}{\partial t} = -\frac{\partial P}{\partial x_i} + \frac{\partial \tau_{ji}}{\partial x_j} + \rho f_i, \tag{2.2}$$

where P is the pressure, τ_{ji} is the viscous stress tensor, and f_i is the body force per unit mass in the x_i direction.

Conservation of energy

The energy equation states that the rate of change of internal energy equals the work done by stresses and the net heat flux of the fluid element, given by,

$$\rho \frac{du}{dt} = \sigma_{ji} \frac{\partial v_i}{\partial x_j} - \frac{\partial q_i}{\partial x_i}, \tag{2.3}$$

where u is the specific internal energy, σ_{ji} is the stress tensor, and q_i is the heat flux vector.

2.2 SST k-ω turbulence model

The simulations utilize the Shear-Stress Transport (SST) k-ω model, which is a two equation turbulence model where k is the turbulent kinetic energy and ω is the specific dissipation rate [29]. The model combines the k-ϵ and k-ω models by taking advantage of the lower sensitivity of k-ϵ in the freestream, while switching to k-ω in the near-wall region to better handle adverse pressure gradients. A blending function is used to transition between the models and to avoid instability from differences in the eddy viscosity formulation. The transport equations for turbulent kinetic energy and the specific dissipation rate are, respectively,

$$\frac{\partial}{\partial t}(\rho k) + \nabla \cdot (\rho k \bar{\mathbf{v}}) = \nabla \cdot [(\mu + \sigma_{k\mu_t})\nabla k] + P_k - \rho\beta^* f_{\beta^*}(\omega k - \omega_{0k0}) + S_k, \tag{2.4}$$

$$\frac{\partial}{\partial t}(\rho \omega) + \nabla \cdot (\rho \omega \mathbf{v}) = \nabla \cdot [(\mu + \sigma_{\omega\mu_t})\nabla \omega] + P_\omega - \rho\beta f_\beta(\omega^2 - \omega_0^2) + S_\omega, \tag{2.5}$$

where ρ is the density, μ is the dynamic viscosity and μ_t is the turbulent eddy viscosity, σ_k and σ_ω are diffusion constants, ω_0 and k_0 are source terms, P_k and P_ω are production terms, β^*, f_{β^*}, β, and f_β are closure constants.
The kinetic energy is given by,

$$k = \frac{3}{2}(UI)^2, \tag{2.6}$$

where U is the mean flow velocity and I the intensity. The turbulent dissipation rate is given by,

$$\omega = \frac{k^{0.5}}{C_\mu^{0.5} l}, \tag{2.7}$$

where C_μ is a turbulence model constant and l the turbulent length scale.

2.3 SIMPLE pressure-velocity coupling algorithm

The Semi-Implicit Method for Pressure-Linked Equations (SIMPLE) is an algorithm used to numerically solve the Navier-Stokes equations [30]. Figure 2.1 illustrates a flowchart for the algorithm in two dimensions. First, an initial guess for the velocities and pressure is made. Step 2 solves the momentum equations for the two velocities using the current pressure field, continuity will not be satisfied at this step. Step 3 solves the pressure correction by enforcing continuity on the velocities. Step 4 updates the pressure and velocities with the new values, and finally the transport equations are updated. The algorithm repeats until convergence has been satisfied.

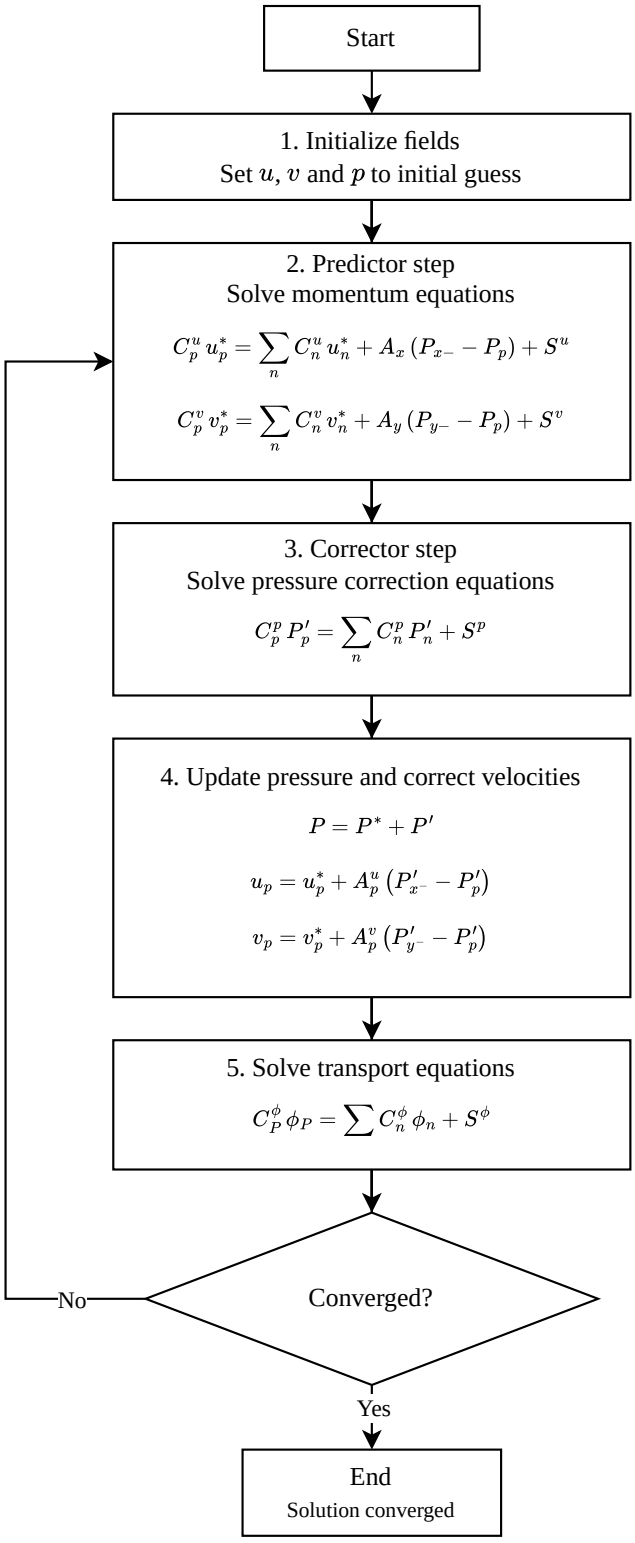

Figure 2.1: Flowchart for the SIMPLE algorithm.

2.4 Wind and force definitions

In sailing, three wind speeds are of interest. The true wind speed (TWS) is the actual wind speed measured relative to a fixed point. The wind induced by the motion of the ship is equal to the speed of the ship but in the opposite direction, is denoted V. The combination of TWS and V produces the apparent wind speed (AWS), which is the wind experienced by an observer moving along with the ship. The relationship between these three wind vectors is illustrated in Fig. 2.2. Both TWS and AWS have their corresponding angles in relation to the heading of the ship, the true wind angle (AWA) and the apparent wind angle (AWA), respectively. In this illustration, the leeway of the ship, the sideways drift caused by the wind pushing on the sails, is not considered.

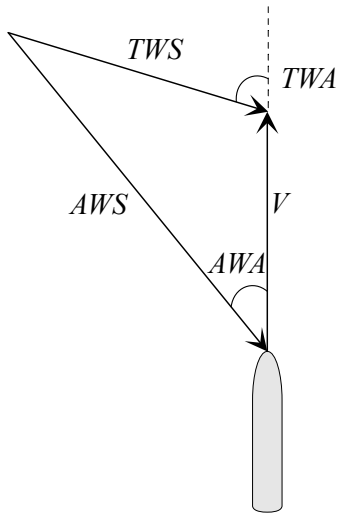

Figure 2.2: The wind velocity triangle.

The AWS is given by,

$$AWS = \sqrt{V^2 + TWS^2 + 2V \cdot TWS \cdot \cos(TWA)}, \tag{2.8}$$

and AWA by,

$$AWA = \arctan\left(\frac{TWS \cdot \sin(TWA)}{V + TWS \cdot \cos(TWA)}\right). \tag{2.9}$$

The two primary forces that act on an airfoil are lift and drag. The lift acts in the direction normal to the approaching wind, whereas the drag acts parallel to it. These force vectors can be decomposed into thrust and side force components. The thrust is the force that propels the ship forward, whereas the side force, acting perpendicular to the ship, induces lateral drift. Figure 2.3 presents a top-view illustration of three wingsails (WS). The coordinates x and y denote stream-wise and normal directions, respectively. α is the angle of attack (AoA), defined as the angle between the apparent wind direction and the chord line. It is adjusted by rotating the wingsails about their quarter chord position. β is the apparent wind angle (AWA), defined as the angle between the direction of the ship and the wind. s is the sheeting angle, defined as the angle between the sail and the centerline of the ship. C_L and C_D are the lift and drag force coefficients, acting in the directions of x and y. C_T and C_S are the thrust and side force coefficients along the ship and perpendicular to the ship, respectively.

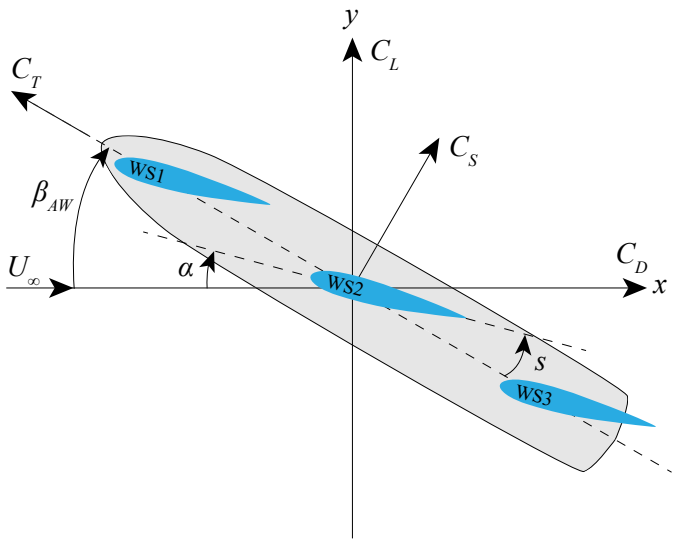

Figure 2.3: Definition of the coordinate system and the acting force coefficients.

2.5 Co-flow jet equations

To correctly calculate the lift and drag forces for a CFJ airfoil, the contribution of the jet must be accounted for in addition to the viscous and pressure forces used for a standard airfoil. This section introduces the equations required for the CFJ force calculations and the methodology to obtain them.

2.5.1 Jet momentum coefficient

To quantify the intensity of the jet, the jet momentum coefficient C_μ is used, defined as,

$$C_\mu = \frac{\dot{m}_j V_j}{0.5 \rho_\infty U_\infty^2 S}, \tag{2.10}$$

where $\dot{m}_j$ is the injected mass flow, V_j is the mass-averaged velocity of the jet, ρ_∞ and U_∞ the density and velocity of the freestream, and S denotes the planform area of the airfoil.

2.5.2 Lift and drag forces

By performing a control volume analysis on the CFJ airfoil, the equations for the reactionary forces generated by the slots can be derived [31]. In Fig. 2.4, the control volume for the CFJ airfoil is illustrated. Applying the momentum equation on this volume gives,

$$\sum \mathbf{F} = \iint_s \rho \boldsymbol{V} \cdot \mathbf{dS} \cdot \boldsymbol{V}. \tag{2.11}$$

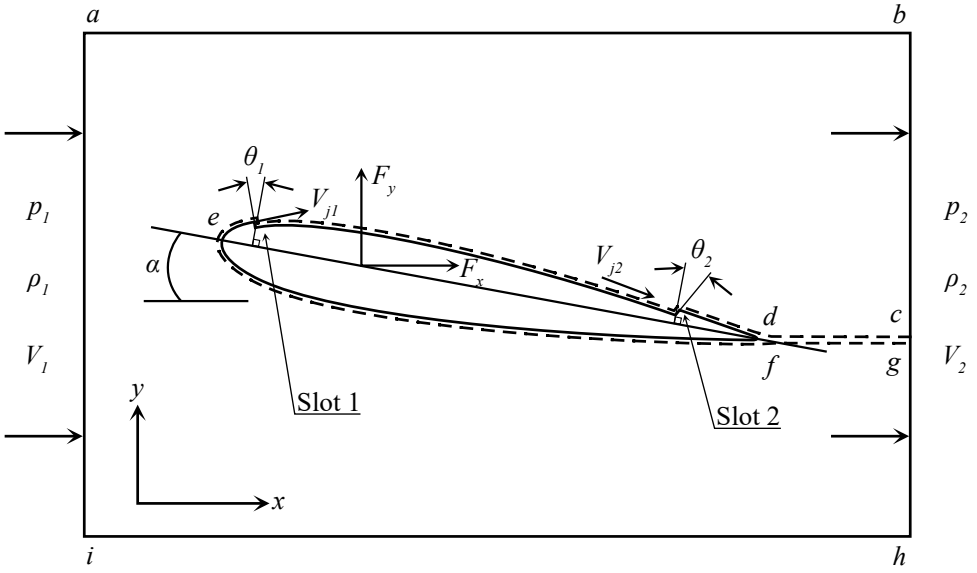

Figure 2.4: Control volume for a CFJ airfoil.

Equation 2.11 describes the resulting force acting on the control volume as a function of the momentum flux through its boundaries. Taking only the x-direction into consideration, one gets,

$$\begin{aligned} &- p_e A_e + p_\infty A_\infty + (p_{j1} A_{j1})_x - (p_{j2} A_{j2})_x + R_x \\ &\quad = \int_h^b \rho V_e \, \mathrm{d}y V_e - \int_i^a \rho V_\infty \mathrm{d}y V_\infty - \dot{m}_{j1} u_{j1} + \dot{m}_{j2} u_{j2}. \end{aligned} \tag{2.12}$$

Here, R_x denotes the pressure and shear stress integral caused by the airfoil in the control volume. Since the freestream pressure and area equal the control volume exit values, $p_e = p_\infty$ and $A_e = A_\infty$, they cancel out the first two terms on the left-hand side of the equation. The reactionary force in the x-direction generated by the slots, $F_{x,CFJ}$, is obtained by applying the momentum equations to a control volume defined between the injection and suction slots,

$$\begin{aligned} F_{x,CFJ} &= [\dot{m}_{j1} u_{j1} + (p_{j1} A_{j1})_x] - \gamma \, [\dot{m}_{j2} u_{j2} + (p_{j2} A_{j2})_x] \\ &= (m_j V_{j1} + p_{j1} A_{j1}) \cdot \cos(\theta_1 - \alpha) - \gamma (m_j V_{j2} + p_{j2} A_{j2}) \cdot \cos(\theta_2 + \alpha), \end{aligned} \tag{2.13}$$

where γ is the suction coefficient. Combining $F_{x,CFJ}$ with the surface drag R_x, the total drag D is obtained using Newton's third law,

$$D = - \left(R_x + F_{x,CFJ} \right) = R'_x - F_{x,CFJ}, \tag{2.14}$$

where $R'_x = -R_x$ is the CFJ airfoil surface pressure and shear stress integral in the x-direction. Substituting Eqs. 2.12 and 2.13 into Eq. 2.14 gives,

$$D = R'_x - F_{x,CFJ} = \int_i^a \rho V_\infty \mathrm{d}y V_\infty - \int_h^b \rho V_e \, \mathrm{d}y V_e. \tag{2.15}$$

Since this is a zero-net-mass-flux method, injection and suction mass flow rates are equal,

$$\dot{m}_{j1} = \dot{m}_{j2}, \tag{2.16}$$

which together with mass conservation across the control volume,

$$\int_i^a \rho V_\infty \, dy = \int_h^b \rho V_e \, dy, \tag{2.17}$$

allows Eq. 2.14 to be simplified to,

$$D = R'_x - F_{x,CFJ} = \int_h^b \rho V_e \left(V_\infty - V_e\right) \, dy. \tag{2.18}$$

In the same manner, the y-direction reaction force is,

$$\begin{aligned} F_{y,CFJ} &= \left[\dot{m}_{j1} v_{j1} + \left(p_{j1} A_{j1}\right)_y\right] - \gamma \left[\dot{m}_{j2} v_{j2} + \left(p_{j2} A_{j2}\right)_y\right] \\ &= \left(\dot{m}_j V_{j1} + p_{j1} A_{j1}\right) \sin(\theta_1 - \alpha) + \gamma \left(\dot{m}_j V_{j2} + p_{j2} A_{j2}\right) \sin(\theta_2 + \alpha), \end{aligned} \tag{2.19}$$

and the total lift is,

$$L = R'_y - F_{y,CFJ}, \tag{2.20}$$

where R'_y is the y-direction surface pressure and shear stress integral. Equations 2.19 and 2.20 give a few insights:

- The injection reduces lift when $v_{j1} > 0$ and increases lift when $v_{j1} < 0$, although its overall effect on lift is small.
- The suction almost always has the effect of decreasing lift due to the $F_{y,CFJ}$ penalty.
- The injection reduces drag due to the jet thrust, while the suction increases drag.
- Despite the individual penalties of suction on lift and drag, the suction enhances circulation, increasing R'_y and reducing R'_x. The net benefit outweighs the penalty, resulting in higher lift, lower drag, and a net performance gain for the CFJ airfoil.

2.5.3 Power consumption

The power consumed by the CFJ micro-compressor is determined by the total enthalpy difference between the injection and suctions slots, respectively,

$$P = \dot{m} \left(H_{t1} - H_{t2}\right), \tag{2.21}$$

where H_{t1} and H_{t2} are the total enthalpy for the injection and suction slots. Using isentropic relations the power can be expressed as,

$$P = \frac{\dot{m} C_p T_{t2}}{\eta} \left(Ptr^{\frac{\gamma-1}{\gamma}} - 1\right), \tag{2.22}$$

where C_p is the specific heat at constant pressure, T_{t2} is the total temperature in the suction slot, η is the efficiency of the micro-compressor and Ptr is the total pressure ratio between the injection and suction slots. To allow for comparison, the power consumption is nondimensionalized to the power coefficient P_c,

$$P_c = \frac{P}{\frac{1}{2}\rho_\infty U_\infty^3 A_{ref}}, \tag{2.23}$$

where A_{ref} is the reference planform area of the airfoil.

2.5.4 Corrected aerodynamic efficiency

The lift-to-drag ratio, also referred to as aerodynamic efficiency, is the lift generated by an airfoil divided by its drag. It is a measure of how effectively it generates lift relative to its drag, and is traditionally defined as,

$$\frac{L}{D}. \tag{2.24}$$

For a CFJ airfoil Eq. 2.24 still applies, but since the CFJ micro-compressor consumes energy this must be accounted for in order to allow a fair comparison. By adding the power coefficient to the denominator in the previous equation, the efficiency is now defined by Eq. 2.25, and is referred to as the corrected aerodynamic efficiency,

$$\left(\frac{L}{D}\right)_c = \frac{C_L}{C_D + P_c}, \tag{2.25}$$

where C_L and C_D include the contributions from both the airfoil surface and the reaction forces from the CFJ slots derived previously. Therefore, the corrected aerodynamic efficiency provides a more comprehensive measure for performance, penalizing configurations that generate high lift through high power consumption [17].

3
Methods

This chapter goes through the methodology used in this thesis, including how the airfoils are designed, how the simulations are set up and the configuration of the mesh.

3.1 Airfoil design

One of the challenges with sailing is that the sails must be able to operate in any wind direction. A traditional yacht sail flexes and adjusts its camber depending on whether the wind comes from port or starboard, this adaptability is not possible with a rigid wingsail. The closest equivalent to a traditional sail would be an asymmetric airfoil, such as the one seen in Fig. 3.1a. However, since the thrust generated by a wingsail is primarily lift-based, the asymmetric shape only allows for positive lift generation in half of the azimuth angles, the first 180 degrees, illustrated in the same figure. Under port side wind, the asymmetric airfoil produces drag and negative lift, hence the thrust will be in an undesirable direction. To overcome this limitation, a symmetric airfoil can be used, which can generate positive lift across all azimuth angles, as shown in Fig. 3.1b.

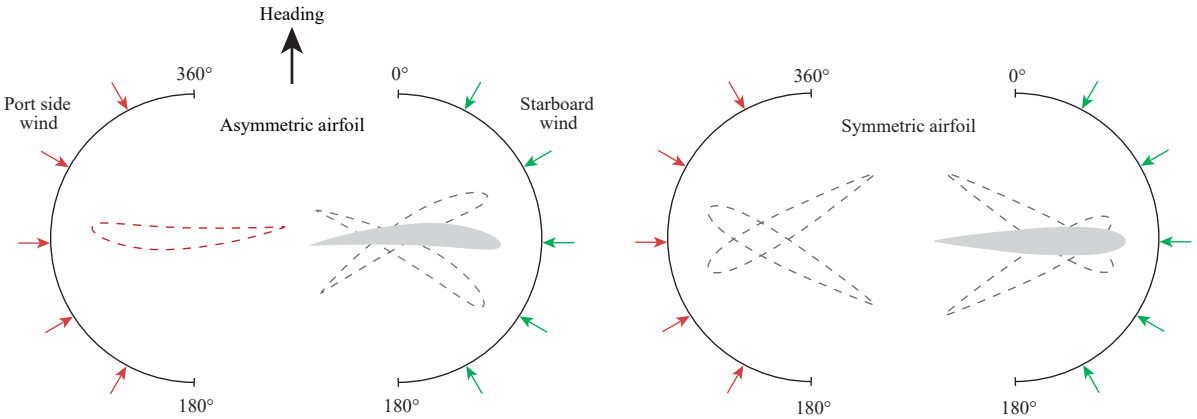

(a) Asymmetric airfoil (b) Symmetric airfoil

Figure 3.1: Working ranges of the asymmetric and symmetric airfoils.

In this study, two different airfoils are used, one standard NACA 0015 and a CFJ variant, which is a modified NACA 0015 with slots for injection and suction.

3.1.1 NACA 0015

For the baseline cases, the NACA 0015 airfoil is used. This profile is employed as a flap element by Oceanbird in their wingsail setup [15]. The NACA 0015 is a symmetric airfoil with a maximum thickness of 15%C. The airfoil geometry is generated by calculating

coordinate points using Eq. 3.1, where t is the maximum thickness, and x and y_t the coordinates. The resulting points are imported into the CAD software, where the geometry is created using a spline function. As the equation does not generate a closed trailing edge, a semicircle is added to enclose the line that shapes the airfoil.

$$y_t = 5t\left(0.2969\sqrt{x} - 0.1260x - 0.3516x^2 + 0.2843x^3 - 0.1015x^4\right) \tag{3.1}$$

Figure 3.2: The NACA 0015 airfoil.

3.1.2 NACA 0015 CFJ

To create an initial CFJ airfoil design, the NACA 0015 was modified to accommodate CFJ requirements. The suction surface is displaced 0.01%C into the airfoil. An injection slot is created at 4%C with a slot size of 0.5%C, and a suction slot at 80%C with a slot size of 0.8%C. To describe the design of the different CFJ airfoils more conveniently, a naming scheme is used. The aforementioned airfoil is designated i04-050-s80-080. To simplify the geometry, the airfoil has injection and suction slots on one side only. In a real world application, the wingsail would have slots on both sides, with the inactive slots closed off by flaps.

Figure 3.3: The NACA 0015 CFJ airfoil.

3.2 Simulation setup

Figure 3.4 illustrates a top-down view of two different wingsail configurations, one with a single sail and the other with three sails. The three-sail configuration has a mast-to-mast spacing of 1.895%C. The ship in the background is added only to facilitate understanding and is not part of the simulations. For a full description of the figures, see Section 2.4.

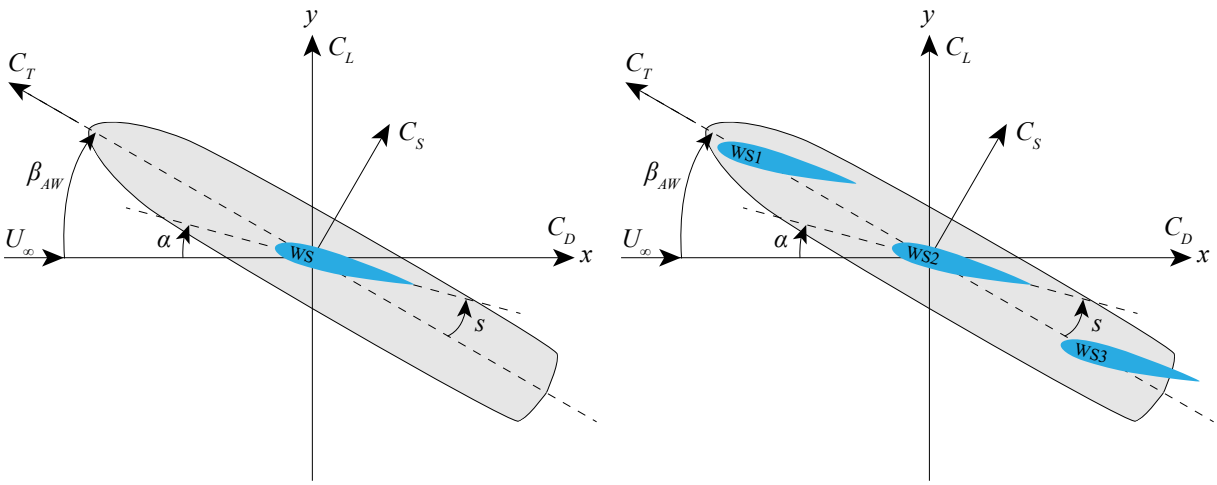

(a) One-sail configuration.

(b) Three-sail configuration.

Figure 3.4: Definitions of the coordinate system and force coefficients for the different configurations.

The micro-compressor that is embedded inside the wingsail, illustrated previously in Fig. 1.2, is not simulated. Instead, it is numerically treated by applying a mass flow inlet boundary condition on the vertical surfaces inside the two slots, as indicated by Fig. 3.5.

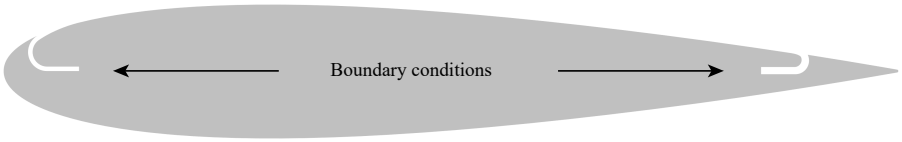

Figure 3.5: NACA 0015 CFJ boundary conditions.

3.2.1 Mesh and boundary conditions

The computational domain consists of a circle with a radius of 30C, and the wingsail is placed with its quarter-chord in the center of the domain. A velocity inlet boundary condition is applied on the left semi-circle, and a static pressure outlet is applied on the right, as seen in Fig. 3.6. The no-slip boundary condition is applied to the wingsail surface. The Reynolds number is 7.35×10^5, corresponding to a freestream velocity of 25 m/s. The domain is meshed with a polygonal mesher with a prism layer. The first layer height is 4.2×10^{-6} m to ensure a Y+ value below one, and the prism layer thickness is set to 3×10^{-6} m to capture the boundary layer. Trailing the wingsail are two wake refinement regions. A finer region with a length of 4C, and a coarser region with a length of 25C.

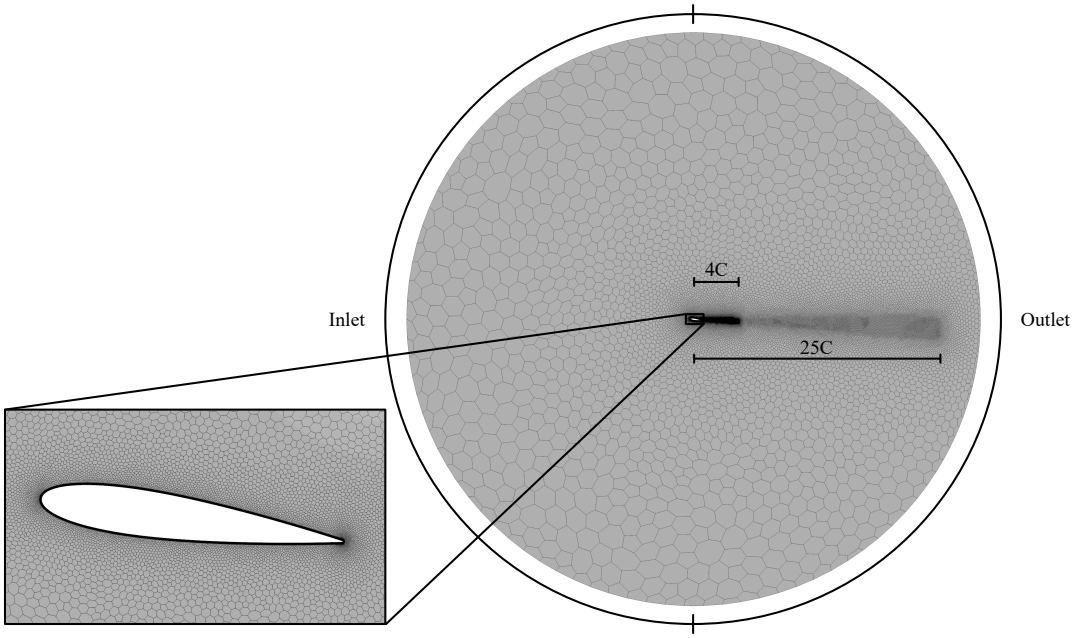

Figure 3.6: The computational domain.

Starting from a baseline mesh of 99217 cells, a finer and a coarser mesh is generated for the mesh independence study, as shown in Figure 3.7. This is achieved by varying the number of points around the airfoil and adjusting the cell size in the whole region by using the base-size adjustment function in the simulation software. As shown in Tab. 3.1, the coarse and fine meshes have a mesh-size variation of about 50%. The C_L and C_D predicted at 8.13° show only minor variation between the meshes, confirming mesh independence and the fact that the initial mesh resolution is sufficient.

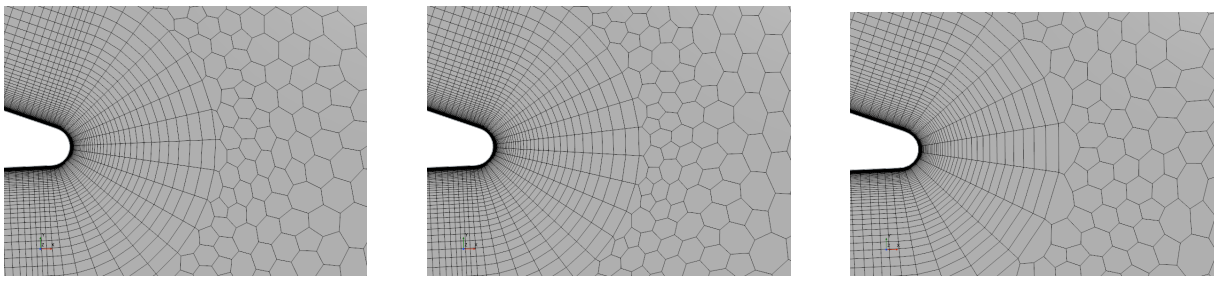

(a) Baseline (b) Fine (c) Coarse

Figure 3.7: Different mesh refinement densities at the trailing edge for a baseline NACA 0015 airfoil.

Table 3.1: Number of cells, lift and drag coefficients for the different meshes.

	Cells	Airfoil faces	C_L	ΔC_L	C_D	ΔC_D
Baseline	99217	861	0.816		0.0181	
Fine	150783	1262	0.818	+0.3%	0.0180	−0.6%
Coarse	53440	464	0.807	−1.1%	0.0185	+2.2%

3.2.2 Solver

The simulations are conducted using the Siemens Simcenter Star-CCM+ CFD software. The flow is modeled in 2D with Unsteady Reynolds-averaged Navier–Stokes (URANS) due to the unsteady nature of the flow. The shear stress transport (SST) k-ω is chosen as a turbulence model. Both the convective and diffusive fluxes are evaluated using a second-order central differencing scheme. The implicit unsteady solver with the second-order Euler implicit scheme is used to approximate the transient term. The physical time step (Δt) is $2{\times}10^{-4}$ s.

4
Results

The results are divided into four parts. The first part validates the baseline airfoil against the experimental data. The second part covers the CFJ airfoil design process, examining parameters such as C_μ and slot locations and sizes. The third part examines a one-sail configuration with CFJ enabled and compares it to a standard airfoil without a lift-enhancing mechanism. Finally, part four builds on the previous part by introducing two additional sails in a three-sail configuration.

4.1 Validation

The setup is validated using experimental wind tunnel data from Ref. [32]. This validation is conducted with a single baseline NACA 0015 airfoil at a Reynolds number of 7.35×10^5, while the experimental data uses a Reynolds number of 6.8×10^5. Figure 4.1 shows a comparison of C_L and C_D over an AoA range of 0° to 20°. For an AoA up to 12°, C_L agrees well with the experimental data. However, as the AoA increases, so does the discrepancy, suggesting URANS's limitation in predicting highly separated flows.

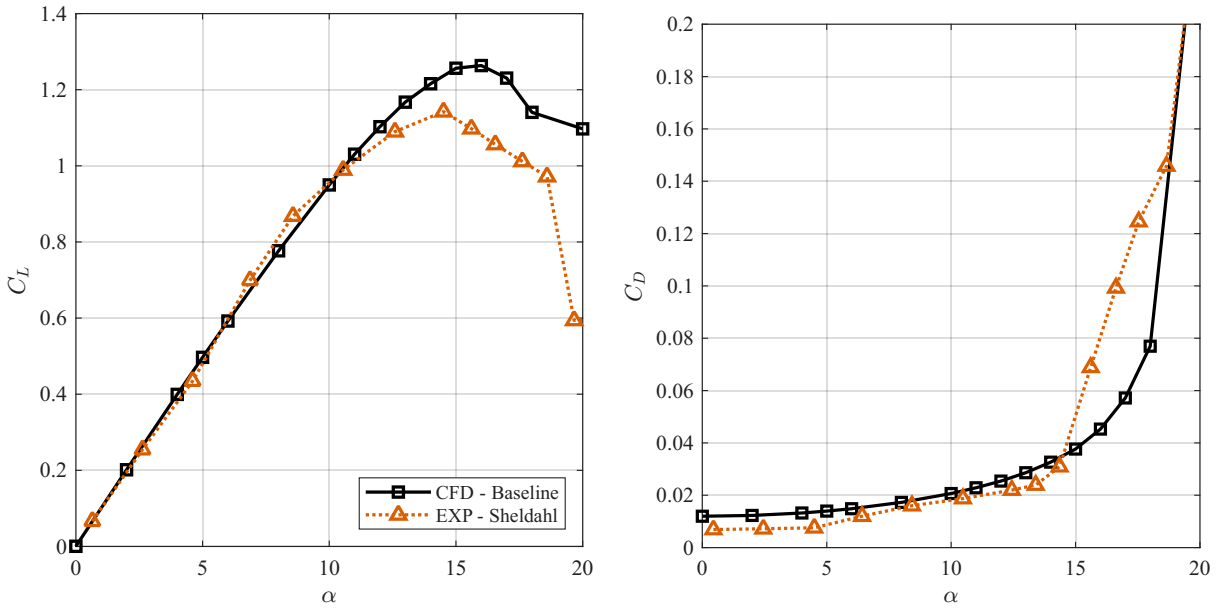

(a) Lift coefficient

(b) Drag coefficient

Figure 4.1: Lift and drag coefficients comparing the CFD and experimental data.

The pressure coefficient distribution (C_p), normalized using Eq. 4.1, is also used for validation. Figure 4.2 shows the C_p distribution at an AoA of 8.13°, which is in good agreement with the experimental data [33].

$$C_p = \frac{p - p_\infty}{0.5\rho_\infty {U_\infty}^2} \tag{4.1}$$

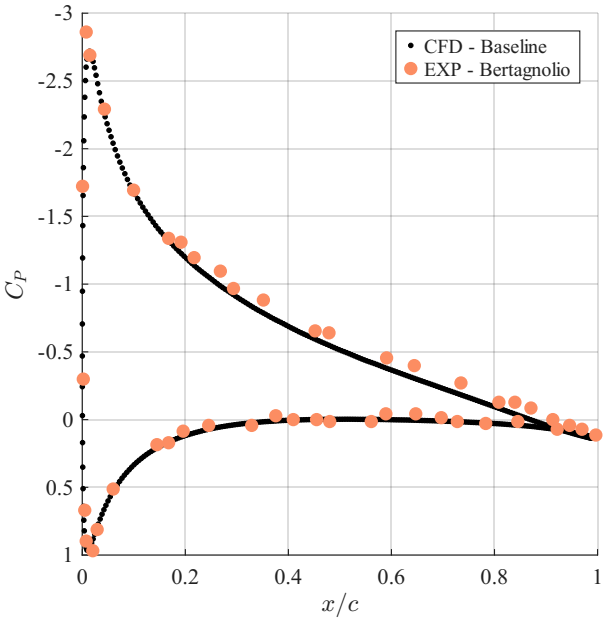

Figure 4.2: Mean pressure coefficient distribution for baseline NACA 0015 at 8.13° AoA.

4.2 Jet momentum coefficient study

To determine a suitable value for C_μ, a parametric study was conducted in which C_μ was varied across different AoA. The AoA was increased in 5° steps between 10° and 35°, while C_μ was varied in increments of 0.025, between 0.050 and 0.125. The airfoil configuration used was the initial design, i05-050-s80-080 (see section 3.1.2 for the naming convention). The results of this study are presented in Fig. 4.3, showing C_L, C_D, P_c and $(C_L/C_D)/_C$ as functions of AoA and C_μ. For the lowest value, C_μ with a value of 0.05, CFJ reaches its maximum C_L before flow separation at the same AoA as baseline, but with a 36% increase in lift and a 36% reduction in C_D. The corresponding P_c is 0.043. The general trend is that increasing C_μ leads to a higher C_L across all AoA. At lower AoA, where the flow remains attached, the increase is relatively low. The primary benefit arises at high AoA, where flow separation is delayed, allowing for operation at a higher AoA and results in a significant lift increase. At lower AoA, the reduction in C_D is likely due to the injected jet, whereas at higher AoA, the dominant contribution to drag reduction is reattachment of the flow. As expected from Eq. 2.23, P_c increases with increasing C_μ across all AoA. For each case, P_c decreases with increasing AoA until flow separation occurs, after which it increases. The conclusion is that a C_μ value of 0.10 provides a good balance between lift enhancement and power consumption. This corresponds to a maximum AoA of 25° before flow separation, representing an increase of 10° compared to baseline. At this condition, C_L increases by 119%, while C_D increases by 40%.

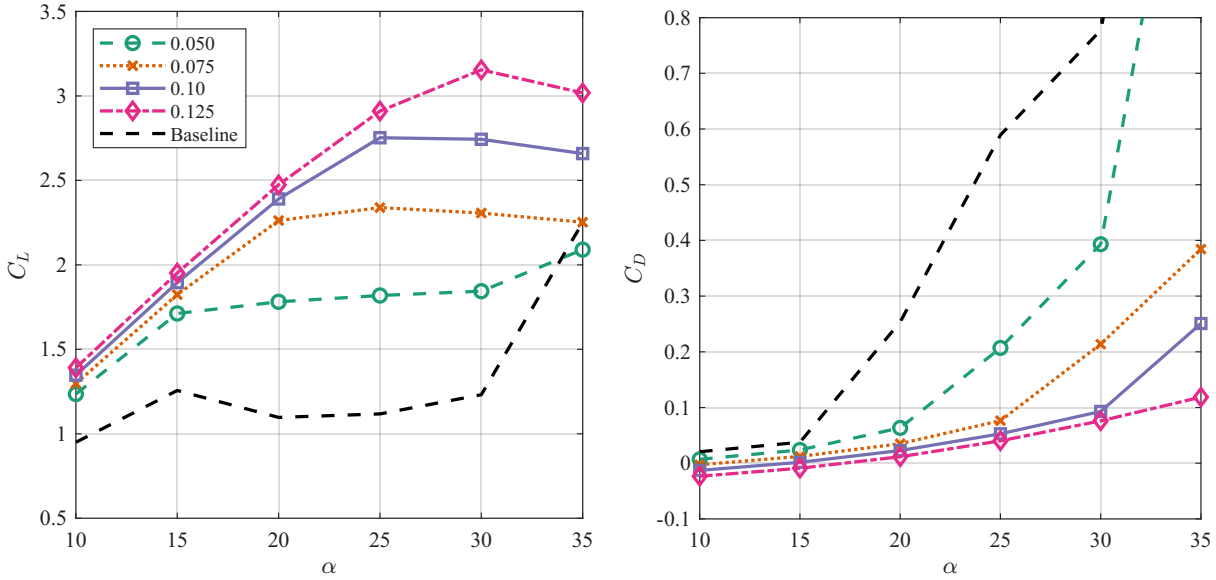

(a) Lift coefficient

(b) Drag coefficient

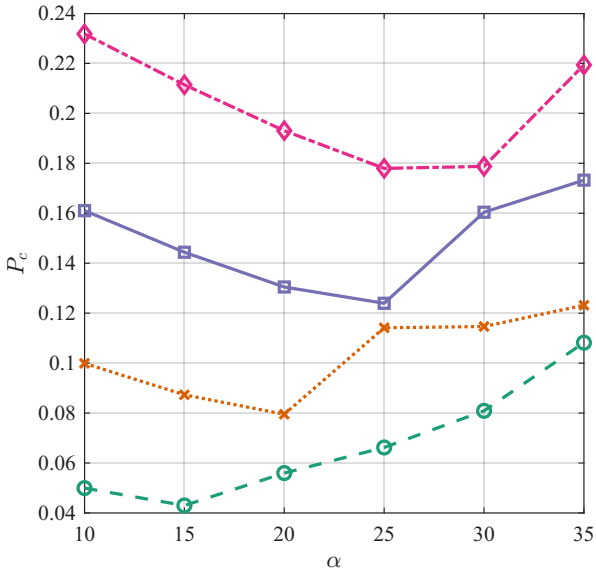

(c) Power coefficient

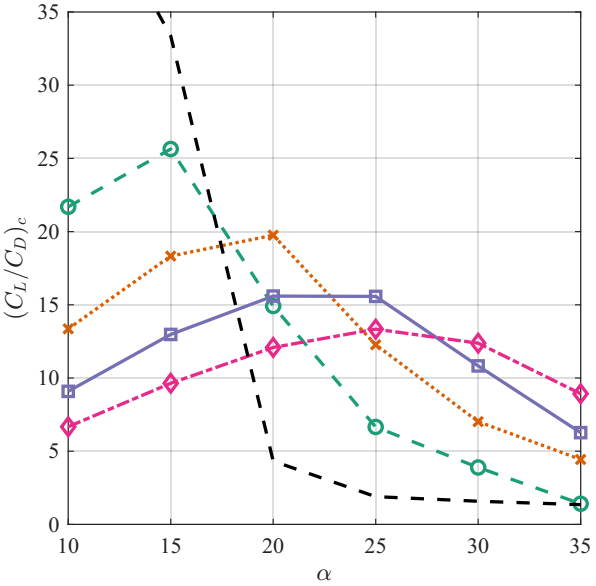

(d) Corrected aerodynamic efficiency

Figure 4.3: Aerodynamic coefficients for variations of C_μ.

4.3 CFJ parametric design study

To investigate the possibility of improving the performance of the CFJ airfoil design, a parametric study was conducted in which the locations and sizes of the injection and suction slots were varied. The initial design had a suction location at 80%C, a suction slot size of 0.8%, an injection slot location at 4%C and an injection slot size of 0.5%C. The C_μ was fixed at 0.1 for all cases, based on the results of the preceding study. An AoA range of 10° to 35° was selected to cover the relevant range before and after stall. Four performance parameters are evaluated, C_L, C_D, P_c and $(C_L/C_D)_c$. Among these, C_L and P_c were considered to be of greatest interest. C_L because the increase in lift is the main contribution to enhancement of thrust, and P_c to assess the efficiency of the system and is therefore desirable to minimize.

4.3.1 Suction slot location study

The first slot study starts with the same airfoil used in the C_μ study, i05-050-s80-080. The location of the suction slot is varied between 75%C, 80%C and 85%C. The results are presented in Fig. 4.5, showing C_L, C_D, P_c and $(C_L/C_D)_c$. Between 10° and 25° AoA, the 85%C slot sees a slight reduction in C_L of 1% or less. However, it achieves a higher maximum C_L of 2.8 at 30° AoA, which is not reached by the other configurations. As shown in Fig. 4.4, having the slot closer to the point of separation appears to be beneficial. At 25°, the 75%C location reduces C_D by 4.7% compared to the 80%C case, P_c is also reduced across the AoA range between 10° and 30°, with a reduction of 1.7% at 25° AoA. In contrast, the 85%C slot increases C_L by 0.8%, but also C_D by 5.1% and P_c by 1.9% at the same AoA. The 75%C location is selected as the most favorable configuration due to its ability to maintain attached flow at a higher AoA while reducing P_c, with a minimal penalty in C_L.

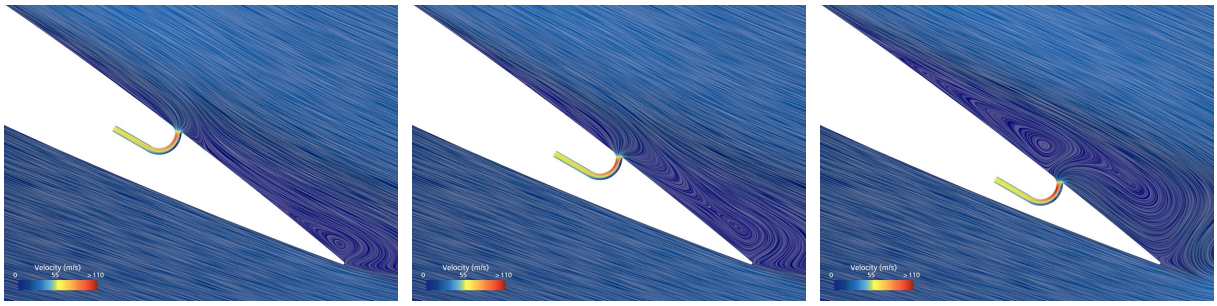

(a) 75%C slot location (b) 80%C slot location (c) 85%C slot location

Figure 4.4: Three different trailing edge slot locations at 30° AoA.

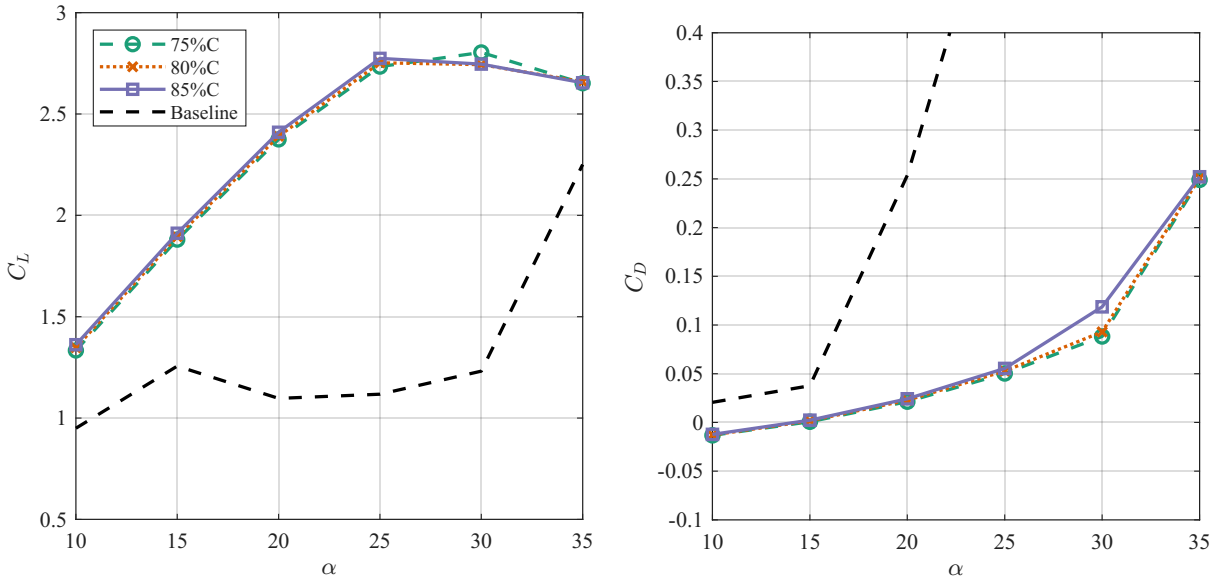

(a) Lift coefficient

(b) Drag coefficient

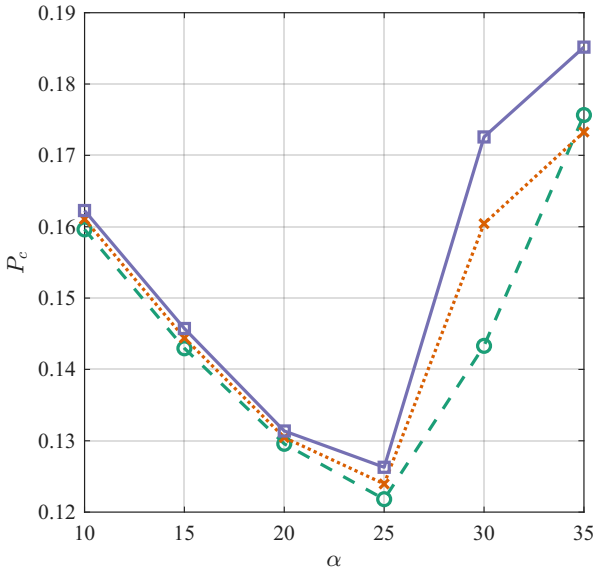

(c) Power coefficient

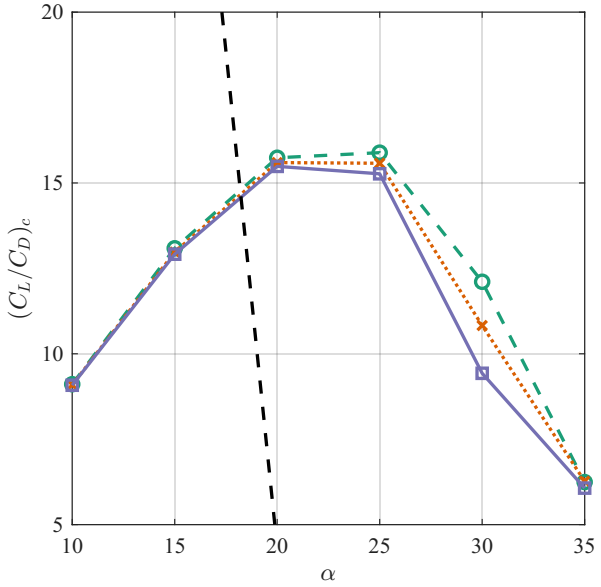

(d) Corrected aerodynamic efficiency

Figure 4.5: Aerodynamic coefficients for the suction slot location study.

4.3.2 Suction slot size study

By adopting the new location selected in the previous study, the airfoil configuration is updated to i05-050-s75-080. In this study, the effect of the suction slot size is investigated by comparing the sizes 0.8%C, 1.2%C and 2.0%C. According to Fig. 4.7a, increasing the slot size has a negligible effect on C_L. At 25°, the increase is within 0.2% for both larger slots compared to the 0.8%C size. In contrast, C_D decreases with 19% and 31% for 1.2%C and 2.0%C configurations, respectively. The slot size has a significant impact on P_c. At 25° AoA, P_c decreases by 13% and 16% for the 1.2%C and 2.0%C sizes, respectively. This large difference can be explained with the term $(Ptr^{\frac{\gamma-1}{\gamma}})$ in Eq. 2.22. As the slot size increases, the velocity within the slot decreases, as indicated by Fig. 4.6, leading to an increase in pressure. This results in a lower pressure ratio, and due to the exponent involving γ, P_c becomes very sensitive to small changes to the compressor inlet pressure. Further studying Fig. 4.6 shows that a larger slot size creates a recirculation region along the upper horizontal and downstream vertical walls within the slot. This suggests the need for a more efficient slot design. Due to the low P_c and small C_D decrease, with a minimal increase in C_L, the 2.0%C slot size is chosen as the best alternative in this study.

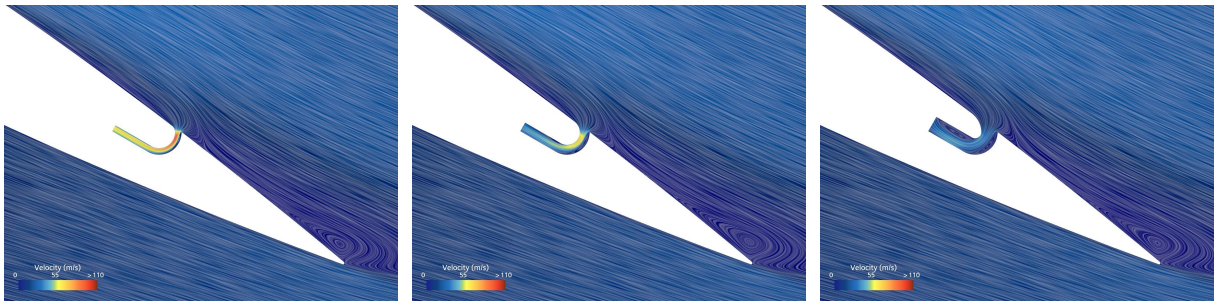

(a) 0.8%C slot size (b) 1.2%C slot size (c) 2.0%C slot size

Figure 4.6: Three different suction slot sizes at 30° AoA.

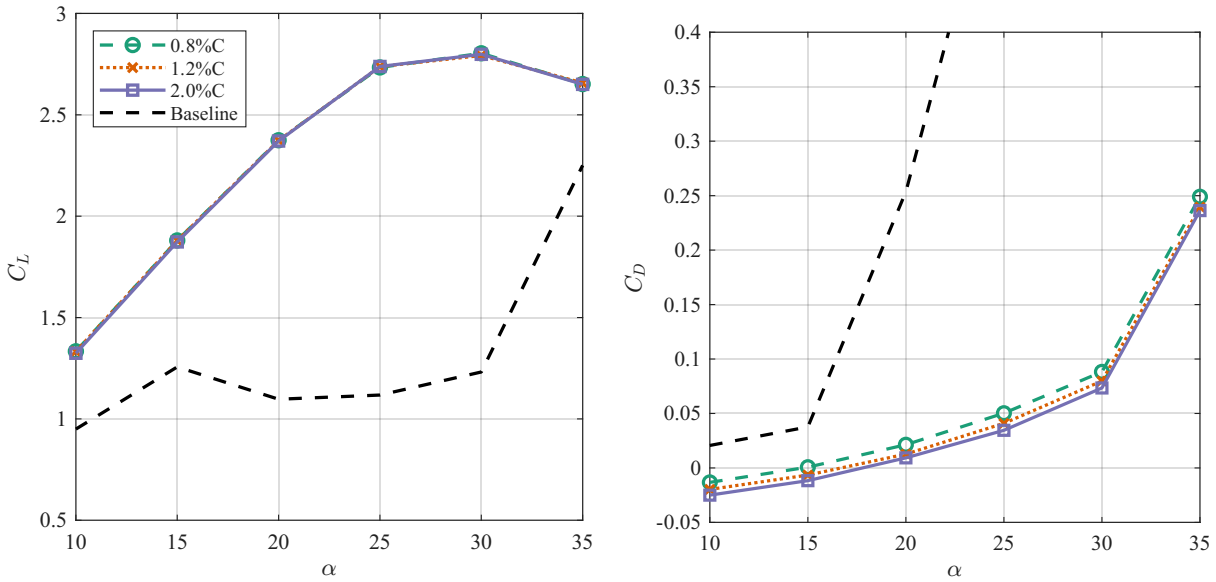

(a) Lift coefficient

(b) Drag coefficient

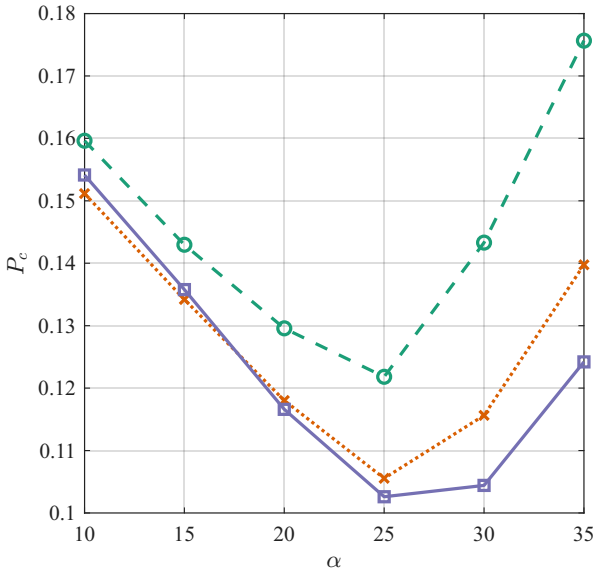

(c) Power coefficient

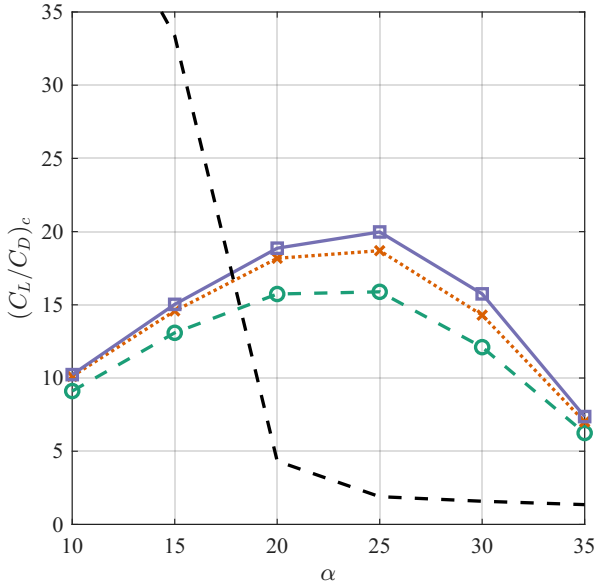

(d) Corrected aerodynamic efficiency

Figure 4.7: Aerodynamic coefficients for the suction slot size study.

4.3.3 Injection slot location study

In this study, the location for the injection slot is investigated at the 3%C, 4%C and 5%C locations. For AoA between 10° and 25°, the 3%C slot location has a reduction of P_c between 2% and 9%, compared to the 4% slot size. In the same range, it has a slight reduction in lift, with a maximum decrease of 1.7%. C_D is marginally higher, with a maximum increase of 13% at 25° AoA. Despite the lower C_L and higher C_D, $(C_L/C_D)_c$ is improved due to the large reduction in P_c. At higher AoA, above 25°, the 3%C configuration reaches its maximum angle before flow separation occurs. In contrast, the 4%C and 5%C configurations maintain attached flow up to 35°, resulting in a higher achievement of C_L. This indicates that positioning the injection slot further downstream is advantageous for higher AoA operations. Focusing on the results at 25° AoA, as done in

the previous slot studies, the the 3%C configuration can be considered the most favorable due to its lower P_c across a wide range of AoA. However, as indicated by the graph in Fig. 4.8a, this configuration operates close to stall. Therefore, the 4%C configuration represents a good alternative for high AoA operations. The illustrations in Fig. 4.9 show a small separation area immediately upstream of the injection slot. Moving the slot downstream further increases the separation.

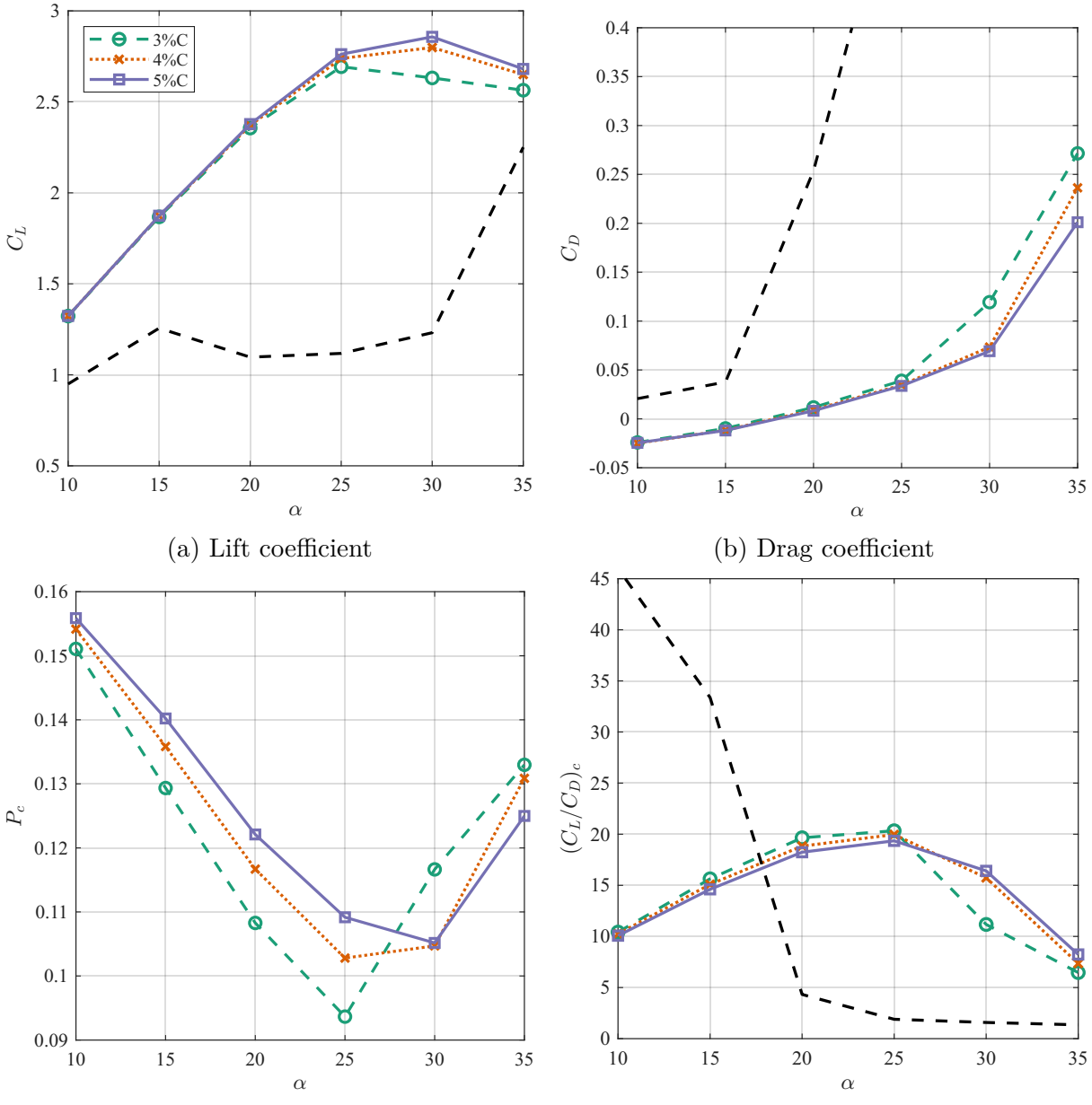

(a) Lift coefficient

(b) Drag coefficient

(c) Power coefficient

(d) Corrected aerodynamic efficiency

Figure 4.8: Aerodynamic coefficients for the injection slot location study.

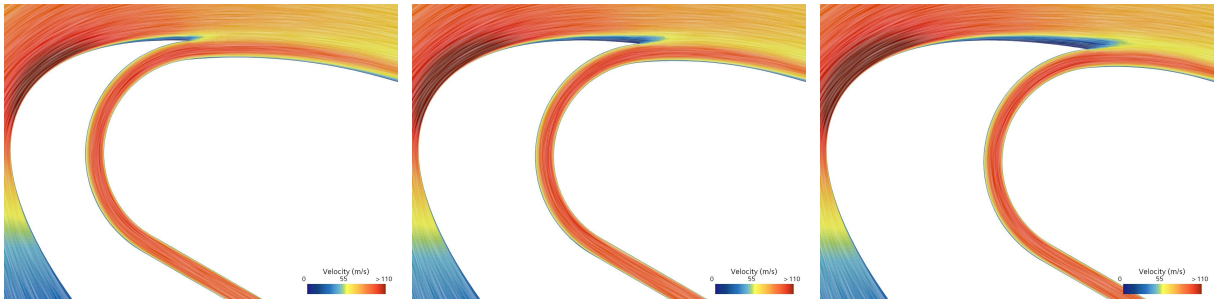

(a) 3%C injection slot location (b) 4%C injection slot location (c) 5%C injection slot location

Figure 4.9: The three different injection slot locations at 30° AoA.

4.3.4 Injection slot size study

In this final configuration study, three injection slot sizes are tested at 0.4%C, 0.5%C and 0.6%C. As shown in Fig. 4.10a, a narrower slot results in a higher maximum C_L and delays stall onset to a higher AoA. At 30° AoA, the 0.4%C slot achieves a C_L of 2.98 with a P_c of 0.13. At 25° AoA, the 0.4%C slot size achieves a C_L of 2.56, which is 14% lower than the 0.6%C configurations, while reducing P_c by 43%. Increasing the slot size leads to a higher mass flow rate but a lower injection velocity, which reduces the required total pressure ratio to power the micro-compressor. According to Eq. 2.22, the power coefficient is linearly dependent on $\dot{m}$ and exponentially dependent on Ptr. As a result, larger slot sizes lead to a reduction in P_c, as shown in Fig. 4.10c. The injection slot size of 0.6%C is selected as optimal due to its balance between low P_C and relatively high C_L, which is reflected in the favorable corrected aerodynamic efficiency shown in Fig. 4.10d.

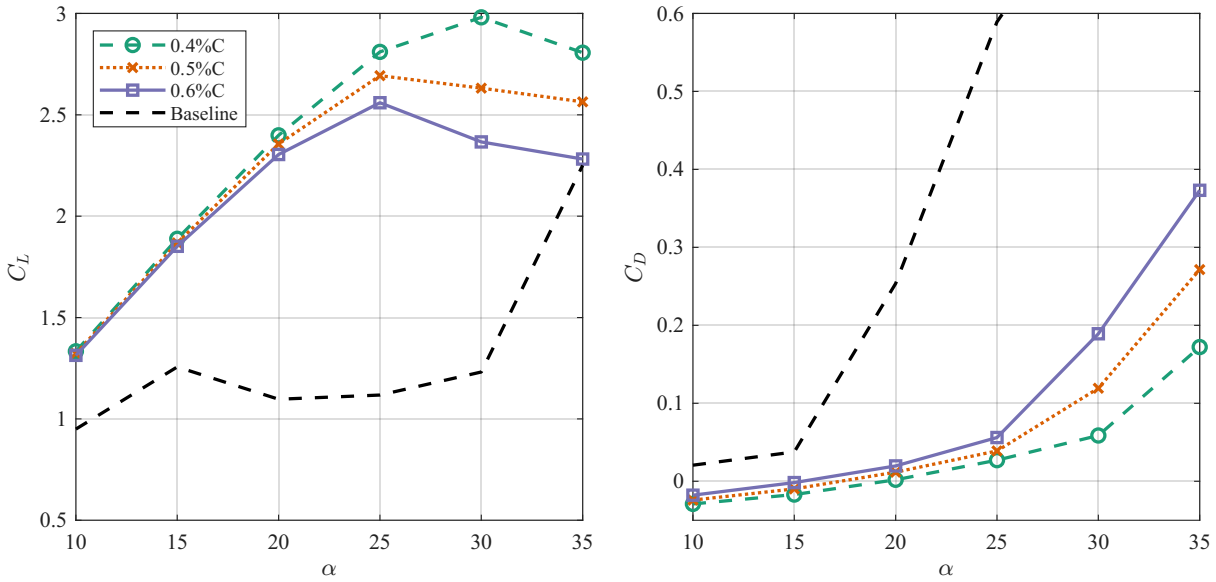

(a) Lift coefficient

(b) Drag coefficient

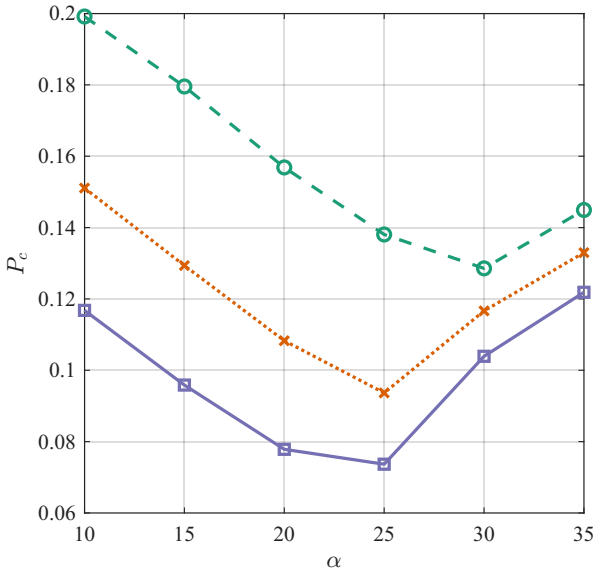

(c) Power coefficient

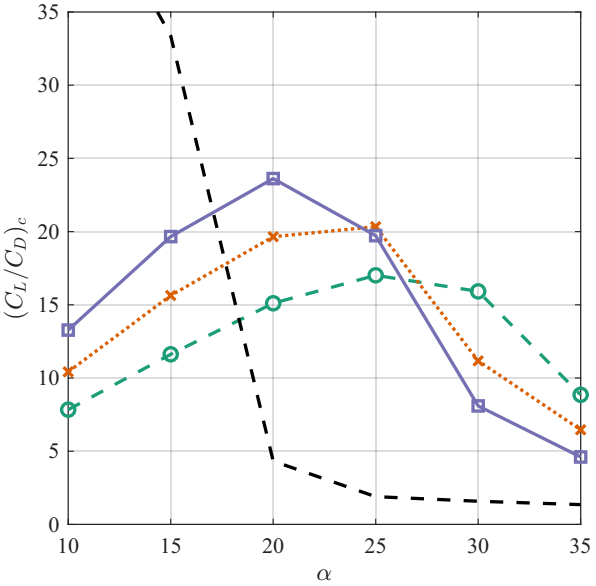

(d) Corrected aerodynamic efficiency

Figure 4.10: Aerodynamic coefficients for the injection slot size study.

The final CFJ airfoil design has the parameters i03-060-s75-200, which compared to the initial design i05-050-s80-080, has both slots enlarged and moved upstream. As a result, C_L is reduced by 7.0% and C_D increased by 6.4%, while P_c is reduced by 40.6% with a $(C_L/C_D)_c$ increase by 26.6%.

4.4 One-sail configuration

The parametric study concluded that the optimal design for the CFJ wingsail has the parameters i03-060-s75-200. It operates at its maximum performance at 25° AoA with a C_μ of 0.1. Compared to the baseline case operating at 15° (maximum C_L), C_L is increased by 104% from 1.26 to 2.56, while C_D is increased by 49%, from 0.038 to 0.056. Figure 4.11 compares the velocity contours of the baseline case at 15° and 25°, together with the CFJ

case at 25° AoA. As shown in Fig. 4.11a, the baseline case has a slight flow separation emanating from the trailing edge. As the AoA increases to 25° the flow separation now extends all the way to the leading edge, covering the entire airfoil. Comparatively, the application of CFJ in the optimum configuration fully attaches the flow at the same AoA, as shown in Fig. 4.11c.

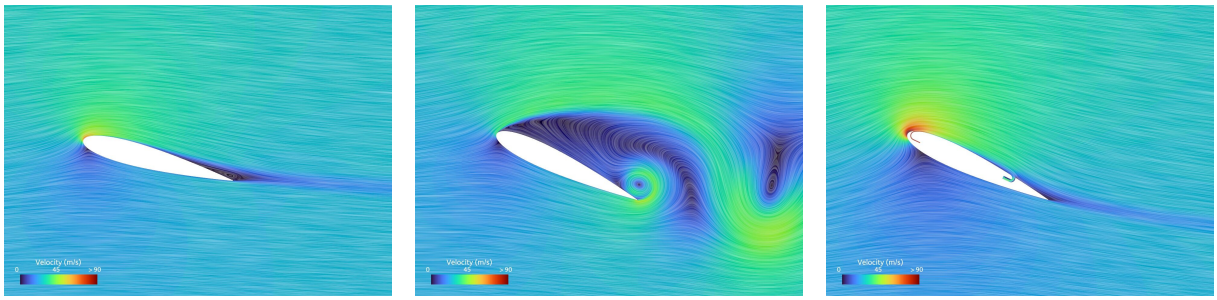

(a) Baseline: 15° (b) Baseline: 25° (c) CFJ: 25°, C_μ of 0.1

Figure 4.11: Comparison between the baseline and CFJ airfoils, with an AoA that corresponds to the optimal AoA determined in the one-sail configuration study.

The aerodynamic performance of the optimal CFJ configuration is projected onto the wingsail performance by plotting the thrust coefficient (C_T) and the power-savings coefficient (PS) on a polar chart as shown in Fig. 4.12. Due to the symmetric nature of the airfoil, only one half of the polar chart is shown. The PS represents how much power is generated by the wingsail propulsion that can be used to offset engine power output for fuel savings. As illustrated in Fig. 3.4a, the AWA represents the heading of the ship relative to the wind. For each AWA in the polar chart, both the baseline and CFJ wingsails are kept at their respective optimal AoA, corresponding to the maximum C_L, 15° and 25°, respectively. C_T is the decomposition of C_L and C_D to the heading of the ship. The total power-savings coefficient, PS_{tot}, is defined as the product of C_T and the non-dimensional sailing velocity, ($\frac{V_s}{V_\infty} = \frac{15}{25}$). The net power-savings coefficient, PS_{net}, is then determined by subtracting the CFJ power consumption, represented by P_c, from PS_{tot}, as given by Eq. 4.2. For quantitative comparison, Tab. 4.1 presents the baseline and CFJ wingsail performance for three typical AWAs. The maximum net power saving is achieved at an AWA of 90°, reaching a value of 93%.

$$PS_{net} = PS_{tot} - P_c \tag{4.2}$$

Table 4.1: Thrust coefficient and net power savings for three different AWA.

	C_T			PS_{net}		
θ_{AW}	BL	CFJ	Δ	BL	CFJ	Δ
30	0.60	1.23	106%	0.36	0.67	86%
90	1.26	2.56	103%	0.76	1.47	93%
150	0.66	1.33	100%	0.40	0.73	82%

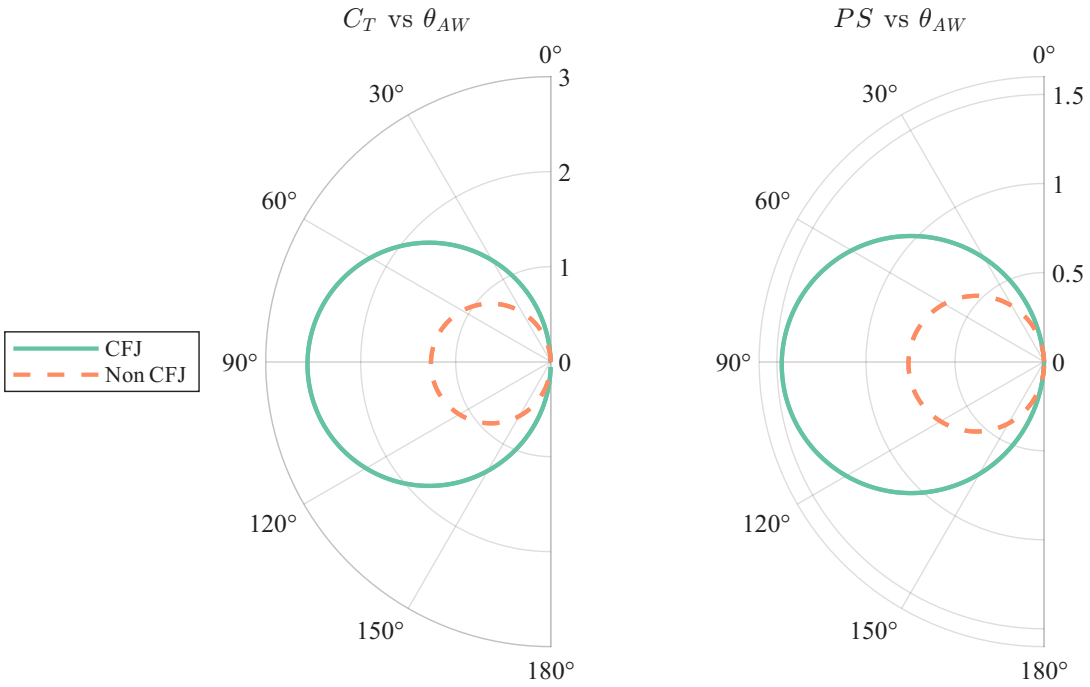

Figure 4.12: Polar plot for the baseline case at 15° AoA and the CFJ case at 25° AoA: variations of C_T (left) and net power saving (right) with AWA.

4.5 Three-sails configuration

This section presents the results of a three-sail configuration at three AWAs, 30°, 90° and 150°. These angles correspond to typical sailing conditions, namely close haul, beam reach, and broad reach. The results are divided into two parts. In the first part, all sails are assigned the same AoA, and for the CFJ cases the same value of C_μ. In the second part, the AoA of each sail is varied independently to fully exploit aerodynamic interaction effects. In addition, C_μ is adjusted individually for each wingsail to achieve flow attachment while minimizing power consumption. A naming convention is used to describe the different configurations. Baseline cases follow the format 'AWA':'AoA WS1'-'AoA WS2'-'AoA WS3', while CFJ cases include the values of C_μ with the addition of CFJ-'C_μ WS1'-'C_μ WS2'-'C_μ WS3'. For example, 30:25-25-25-CFJ-10-10-10, represents an AWA of 30°, with all three sails operating at an AoA of 25° together with a C_μ of 0.10 for all three sails.

4.5.1 30° apparent wind angle

4.5.1.1 Uniform AoA and C_μ at 30° AWA

Figure 4.13 compares the baseline and CFJ wingsail configurations with AoA fixed at 15° and 25°. For the baseline case shown in Fig. 4.13a, flow separation occurs on WS1, is significantly reduced on WS2 and is absent on WS3. The results in section 4.1 suggested that a single NACA 0015 airfoil experiences a near stall condition at 15° AoA but should not expect an obvious flow separation as shown in Fig. 4.13a. The presence of the downstream sails WS2 and WS3 pushes the wake of WS1 upward, causing WS1 to experience an upwash effect and consequently an increased effective AoA beyond 15°. In contrast, WS2

and WS3 are immersed in the downwash effect induced by WS1, resulting in a reduced effective AoA and delayed or suppressed separation. This behavior is further illustrated in Fig. 4.14, which presents the C_p distributions of the three sails for the baseline 30:15-15-15 case. The stagnation points, highlighted in the zoomed in view, are located in successive order downstream from WS1 to WS3. This location distribution aligns with the change of AoA, which is evidence of the aforementioned upwash and downwash effects. To suppress separation on WS1, CFJ is applied with a C_μ value of 0.3, corresponding to an average value of 0.1 across all three sails. As shown in Fig. 4.13b, a high-energy jet is injected from the injection slot and completely removes the flow separation. As a result, C_L is increased by 26% and C_D is reduced by 97%. However, this also strengthen the downwash effect on WS2 and WS3. Increasing the AoA from 15° to 25°, the flow remains attached on WS1 but separates on WS2 and WS3, indicating that enabling CFJ only on the leading sail is insufficient. Distributing C_μ uniformly across all three sails with a value of 0.1 leads to separation on WS1, but eliminates it on WS2 and WS3, as shown in Fig. 4.13d. In this case the average C_L is increased by 17% while P_c is reduced by 79%. Overall, the results demonstrate that at an AWA of 30°, the interaction effects are strong. Upwash increases the loading and stall tendency of upstream sails, while downwash delays stall on downstream sails. The variation of C_μ and AoA for individual sails will therefore follow the patterns of interaction effect to best exploit it for performance improvement.

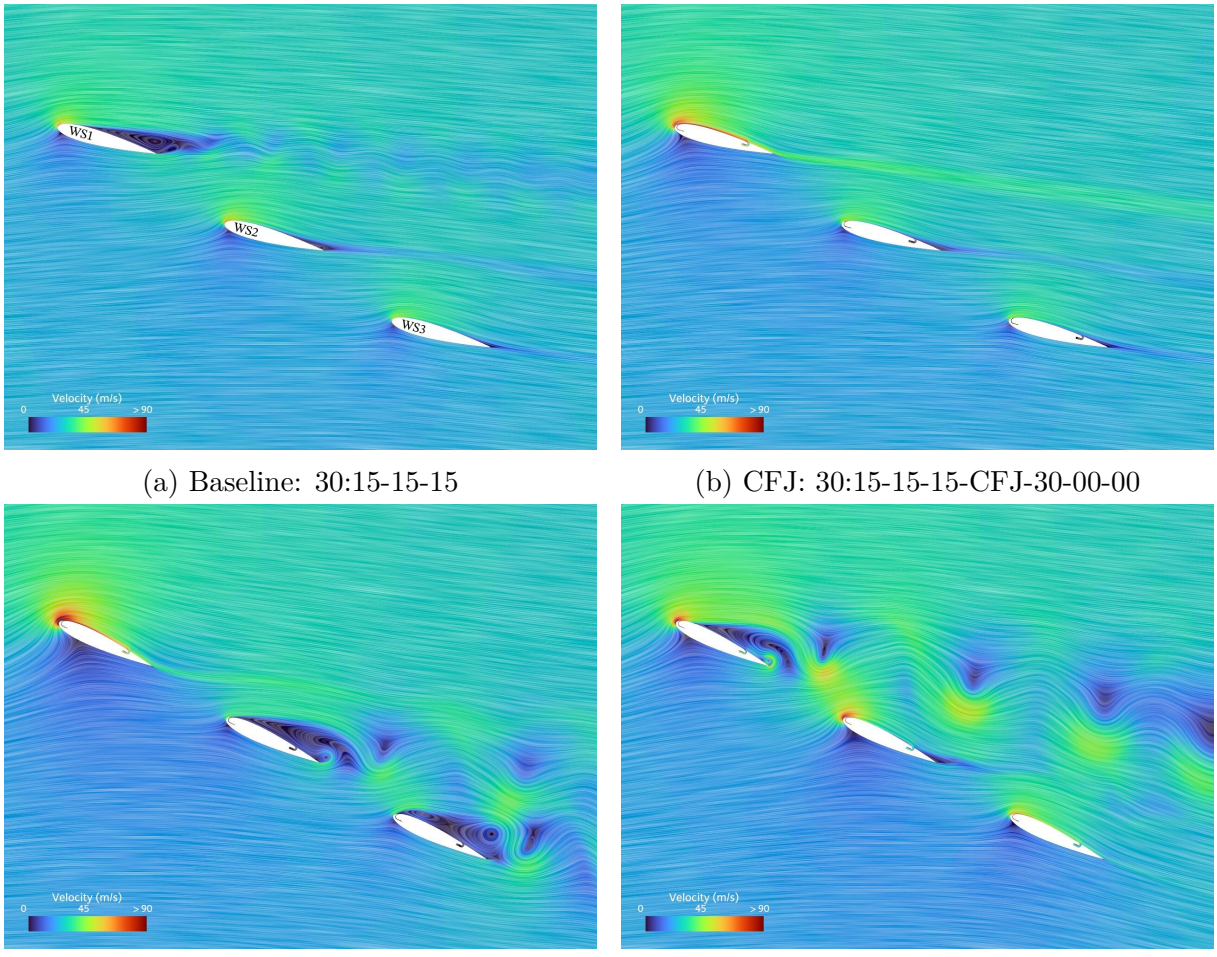

(a) Baseline: 30:15-15-15

(b) CFJ: 30:15-15-15-CFJ-30-00-00

(c) CFJ: 30:25-25-25-CFJ-30-00-00

(d) CFJ: 30:25-25-25-CFJ-10-10-10

Figure 4.13: Different baseline and CFJ configurations with a uniform AoA at 30° AWA.

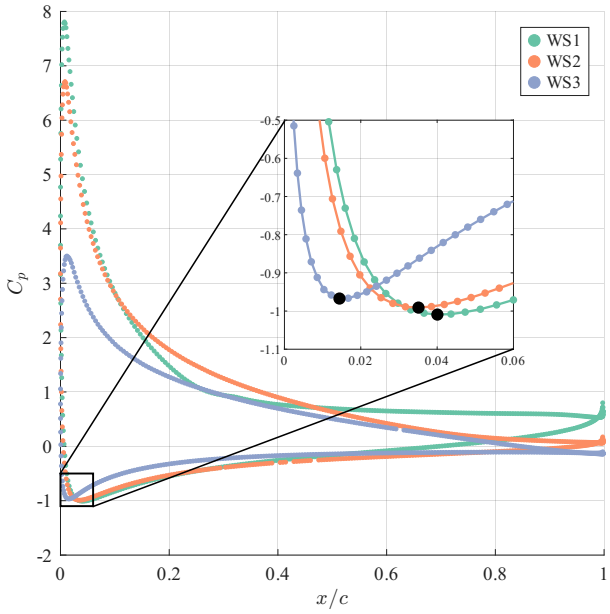

Figure 4.14: Pressure coefficient distributions together with stagnation points for the baseline 30:15-15-15 case.

Table 4.2: Performance data for uniform cases at 30° AWA.

	WS	15-15-15	15-15-15	25-25-25	25-25-25
C_μ	1	-	0.3	0.3	0.1
	2	-	-	-	0.1
	3	-	-	-	0.1
	Avg.	-	0.1	0.1	0.1
C_L	1	1.42	2.85	3.96	2.76
	2	1.38	1.05	0.98	2.38
	3	0.94	0.80	0.82	1.61
	Avg.	1.25	1.57	1.92	2.25
C_D	1	0.051	-0.230	-0.278	0.25
	2	0.049	0.124	0.415	0.12
	3	0.105	0.110	0.432	0.319
	Avg.	0.068	0.002	0.190	0.228
C_T	1	0.67	1.63	2.22	1.17
	2	0.65	0.42	0.13	1.09
	3	0.38	0.31	0.03	0.53
	Avg.	0.57	0.78	0.80	0.93
C_S	1	1.26	2.36	3.29	2.52
	2	1.22	0.97	1.05	2.12
	3	0.87	0.75	0.92	1.55
	Avg.	1.12	1.36	1.76	2.06
P_c	1	-	0.620	0.524	0.140
	2	-	-	-	0.086
	3	-	-	-	0.104
	Avg.	-	0.620	0.524	0.110

4.5.1.2 Variable AoA and C_μ at 30° AWA

Figure 4.15 illustrates the effect of varying AoA among the three sails in the baseline case. Reducing the AoA of WS1 by 5° prevents flow separation and results in an increase in C_L

of 6.3%, as shown in Table 4.3. By exploiting the downwash effect from the leading sails, the AoA of WS3 can be increased to 20° while maintaining nearly fully attached flow, as shown in Fig. 4.15b. This higher AoA on WS3 in turn enhance the upwash effect for the upstream wingsails, WS1 and WS2, leading to a significant increases in their C_L. Overall, varying the AoA for WS1 and WS3 in the 30:10-15-20 case, increases the C_L by 12% and decreases C_D by 30%, which results in an C_T increase of 16%. An interesting phenomenon observed when the flow remains attached on all three sails is that C_D becomes negative for WS1. This behavior has also been reported in a study of a tandem airfoil configuration under specific AoA conditions [34].

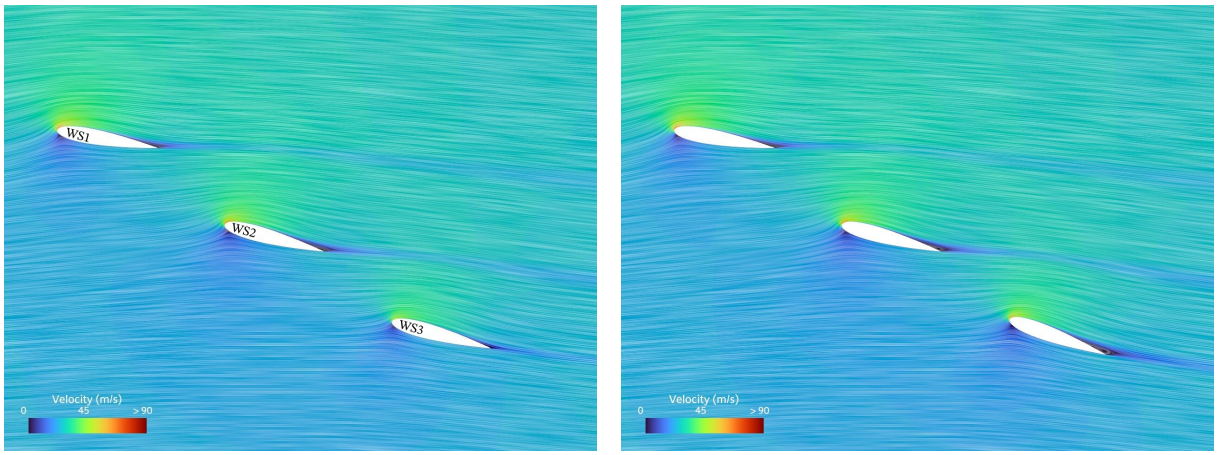

(a) Baseline: 30:10-15-15 (b) Baseline: 30:10-15-20

Figure 4.15: Baseline case with varied AoA at AWA of 30°.

Table 4.3: Performance data for variable baseline cases at 30° AWA.

	WS	15-15-15	10-15-15	10-15-20
C_L	1	1.42	1.51	1.56
	2	1.38	1.37	1.44
	3	0.94	0.93	1.19
	Avg.	1.25	1.27	1.40
C_D	1	0.051	-0.055	-0.065
	2	0.049	0.066	0.060
	3	0.105	0.106	0.149
	Avg.	0.068	0.039	0.048
C_T	1	0.67	0.80	0.83
	2	0.65	0.63	0.67
	3	0.38	0.38	0.47
	Avg.	0.57	0.60	0.66
C_S	1	1.26	1.28	1.31
	2	1.22	1.22	1.27
	3	0.87	0.86	1.11
	Avg.	1.12	1.12	1.23

To improve CFJ three-sail performance at 30° AWA, the first case shown in Fig. 4.16a retains an uniform AoA while redistributing C_μ, keeping the average value constant. WS1 has its C_μ increased to 0.17, while it is reduced to 0.08 and 0.05 for WS2 and WS3, respectively. This redistribution successfully reattach the flow on all three sails, resulting in a 9% increase in C_T and a 25% reduction in P_c compared to the initial uniform

distribution. Resulting in both a higher effectiveness and efficiency. The reduction in P_c is attributed to the decrease in CFJ power consumption in WS2 and WS3, outweighing the increased demand on WS1. Based on this case, further performance gains are explored by varying both AoA and C_μ to better benefit from the interaction effects. Fig. 4.16b shows the configuration 30:20-25-30-CFJ-13-09-08 with both AoA and C_μ reduced for WS1 and increased for WS2 and WS3, resulting in a further increase in C_T. The well-attached flow on WS3 suggests potential for further increasing its AoA. However, increasing the AoA of WS3 to 35° (Fig. 4.16c), induces flow separation on WS1, resulting in a loss of thrust across all sails. This issue is mitigated by decreasing the AoA of WS1 to 15°, as shown in Fig. 4.16d. The final configuration, 15-25-35-CFJ-13-09-08, is considered optimal as it achieves the highest C_T and lowest P_c. These results highlight an important strategy for maximizing the performance of multiple wingsails by taking advantage of interaction effects in close haul conditions. The upstream sails should operate with a higher C_μ and a reduced AoA, while the downstream sails benefit from a lower C_μ and an increased AoA. This approach enables an efficient distribution of C_μ, avoiding over- and under-actuation, and thereby maximizing the net performance gains. Compared to the best baseline configuration at 30° AWA, the CFJ achieves an 89% increase in C_T.

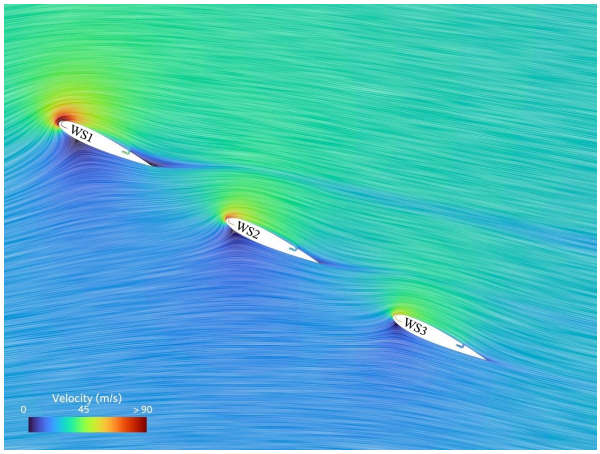

(a) CFJ: 30:25-25-25-CFJ-17-08-05

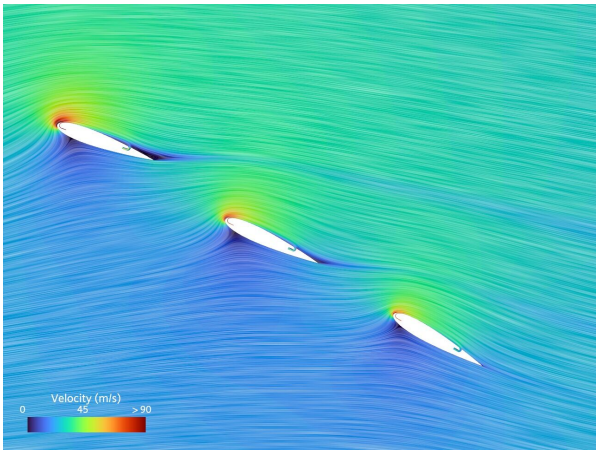

(b) CFJ: 30:20-25-30-CFJ-13-09-08

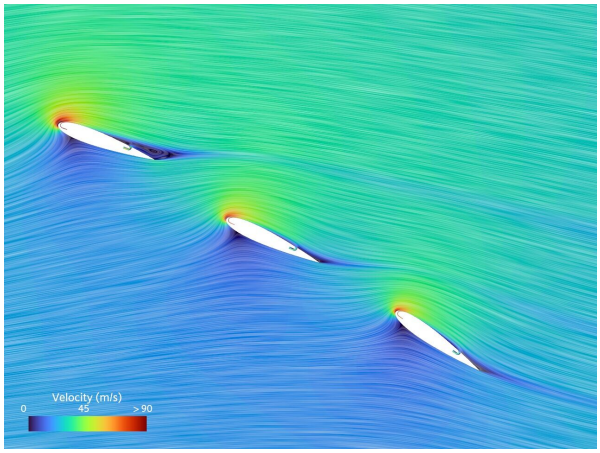

(c) CFJ: 30:20-25-35-CFJ-13-09-08

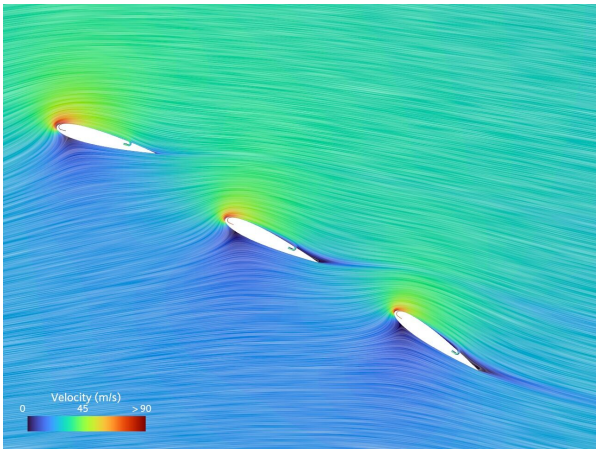

(d) CFJ: 30:15-25-35-CFJ-13-09-08

Figure 4.16: CFJ configurations with variable AoA and C_μ at 30° AWA.

Table 4.4: Coefficients for CFJ with variable AoA and C_μ at 30° AWA.

	WS	25-25-25	25-25-25	20-25-30	20-25-35	15-25-35
C_μ	1	0.10	0.17	0.13	0.13	0.13
	2	0.10	0.08	0.09	0.09	0.09
	3	0.10	0.05	0.08	0.08	0.08
	Avg.	0.10	0.10	0.10	0.10	0.10
C_L	1	2.76	3.85	3.40	3.37	3.27
	2	2.38	2.33	2.60	2.57	2.62
	3	1.61	1.50	1.99	2.09	2.12
	Avg.	2.25	2.56	2.66	2.67	2.67
C_D	1	0.249	-0.303	-0.296	-0.293	-0.357
	2	0.118	0.247	0.182	0.176	0.171
	3	0.319	0.314	0.411	0.481	0.469
	Avg.	0.228	0.086	0.099	0.121	0.094
C_T	1	1.17	2.19	1.96	1.94	1.94
	2	1.09	0.95	1.14	1.13	1.16
	3	1.09	0.48	0.64	0.63	0.65
	Avg.	1.11	1.21	1.25	1.23	1.25
C_S	1	2.52	3.18	2.80	2.77	2.65
	2	2.12	2.14	2.34	2.31	2.35
	3	1.55	1.46	1.93	2.05	2.07
	Avg.	2.06	2.26	2.36	2.38	2.36
P_c	1	0.140	0.170	0.126	0.130	0.108
	2	0.086	0.050	0.062	0.067	0.067
	3	0.104	0.026	0.055	0.062	0.060
	Avg.	0.110	0.082	0.081	0.086	0.078

4.5.2 90° apparent wind angle

4.5.2.1 Uniform AoA and C_μ at 90° AWA

At an AWA of 90°, the interactions between the sails are significantly weaker than at 30°, as the three sails are located in the same streamwise position. For the baseline 90:15-15-15 case shown in Fig. 4.17a, the flow remains attached on all three sails, indicating that this configuration represents an optimal operating condition, as any increase likely would result in flow separation. At 90° AWA, C_L aligns with C_T, while C_S aligns with C_D. Therefore, only one of each is presented in Table 4.5. Increasing the AoA to 25° for the baseline configuration causes significant flow separation on all three sails, resulting in a loss of aerodynamic performance. This can be largely mitigated by enabling CFJ with a uniform distribution of C_μ with a value of 0.1, which significantly reduces the flow separation on WS1 and fully attaches the flow on WS2 and WS3. This indicates that the interaction effects still exist despite the aligned configuration of the sails. Each sail induces a local upwash on the sail adjacent to its suction side and a downwash on the sail adjacent to its pressure side. As a result, the flow attachment improves progressively from WS1 to WS3 under the same C_μ. The aerodynamic performance of the different configurations is presented in Table 4.5. To further optimize the CFJ sails, individual adjustments of AoA and C_μ for each sail are required.

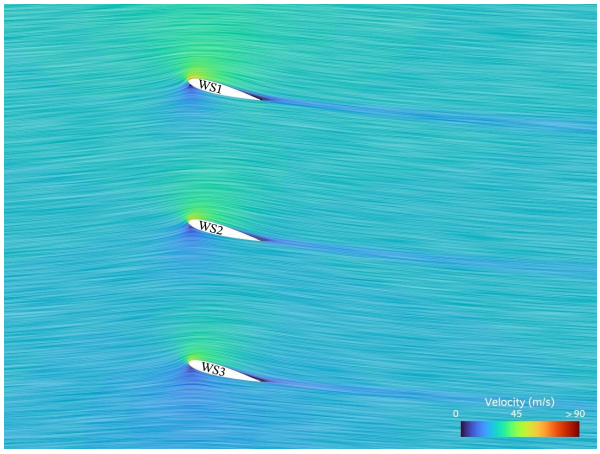

(a) Baseline: 90:15-15-15

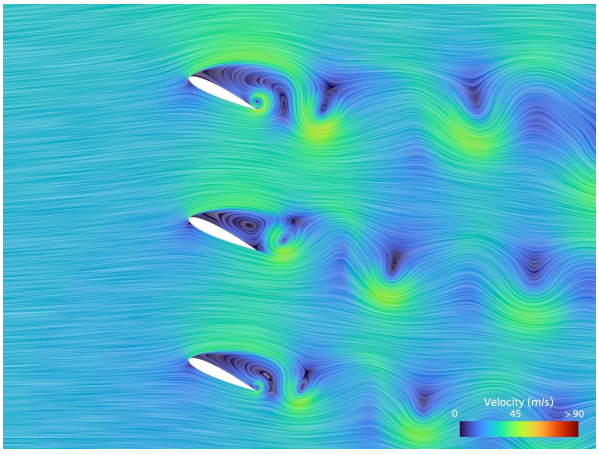

(b) Baseline: 90:25-25-25

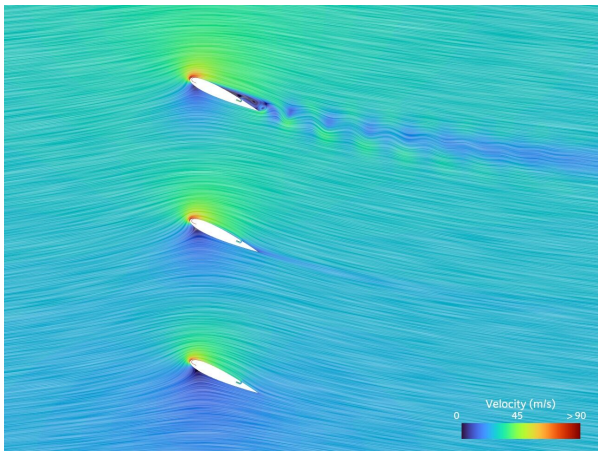

(c) CFJ: 90:25-25-25-CFJ-10-10-10

Figure 4.17: Baseline and CFJ configurations with uniform AoA and C_μ at 90° AWA.

Table 4.5: Coefficients for the uniform configurations at 90° AWA.

	WS	15-15-15	25-25-25	25-25-25
C_μ	1	-	-	0.10
	2	-	-	0.10
	3	-	-	0.10
	Avg.			0.10
C_L, C_T	1	1.38	1.27	2.60
	2	1.18	1.12	2.43
	3	1.05	0.95	1.96
	Avg.	1.20	1.11	2.33
C_D, C_S	1	0.041	0.676	0.166
	2	0.040	0.603	0.084
	3	0.041	0.508	0.055
	Avg.	0.041	0.596	0.102
P_c	1	-	-	0.101
	2	-	-	0.070
	3	-	-	0.083
	Avg.			0.085

4.5.2.2 Variable AoA and C_μ at 90° AWA

Fig. 4.18 presents the CFJ configurations with varying AoA and C_μ. The first case, shown in Fig. 4.18a, attempts to reattach the flow by only redistributing C_μ among three sails. A C_μ distribution of 0.15, 0.08, and 0.07 successfully achieves full flow attachment, resulting in a 3.4% increase in C_T and a 9.4% reduction in P_c compared to the uniform CFJ case with a C_μ of 0.1. Based on this, the AoA of WS3 is further increased while C_μ is redistributed, with a reduced value for WS1 and higher values for WS2 and WS3. This adjustment leads to an additional improvement in aerodynamic performance. Compared to the baseline configuration at AWA 90°, the optimized CFJ case achieves a 108% increase in C_T.

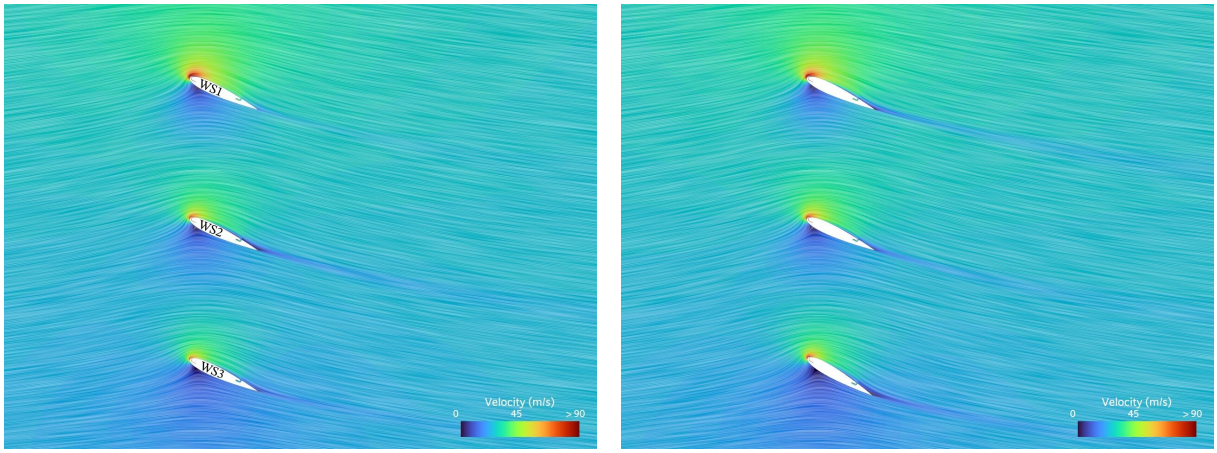

(a) CFJ: 90:25-25-25-CFJ-15-08-07 (b) CFJ: 90:25-25-30-CFJ-12-09-09

Figure 4.18: CFJ configurations with variable AoA and C_μ at 90° AWA.

Table 4.6: Coefficients for CFJ configurations at 90° AWA, with variable AoA and C_μ.

	WS	25-25-25	25-25-25	25-25-30
C_μ	1	0.10	0.15	0.12
	2	0.10	0.08	0.09
	3	0.10	0.07	0.09
	Avg.	0.10	0.10	0.10
C_L, C_T	1	2.60	3.35	3.14
	2	2.43	2.12	2.29
	3	1.96	1.77	2.06
	Avg.	2.33	2.41	2.49
C_D, C_S	1	0.166	0.074	0.097
	2	0.084	0.079	0.080
	3	0.055	0.068	0.089
	Avg.	0.102	0.074	0.089
P_c	1	0.101	0.136	0.094
	2	0.070	0.054	0.060
	3	0.083	0.042	0.065
	Avg.	0.085	0.077	0.073

4.5.3 150° apparent wind angle

4.5.3.1 Uniform AoA and C_μ at 150° AWA

The third AWA of interest is 150°, selected to examine sail interactions under broad reach conditions. In this wind direction, C_D contributes positively to C_T. The baseline configuration shown in Fig. 4.19a, reveals that flow separation is most severe on WS3 and gradually decreases on WS2 and WS1. Increasing the AoA to 25° results in severe flow separation on all three sails, accompanied with significant vortex shedding. Enabling CFJ with a uniform C_μ distribution of 0.1 reattaches the flow on WS1 and WS2, but not on WS3. Despite this limitation, the CFJ configurations achieves a 123% increase in C_T compared to the baseline case. These results indicate that further optimization of both AoA and C_μ is necessary for the baseline and CFJ configurations to fully exploit their potential performance.

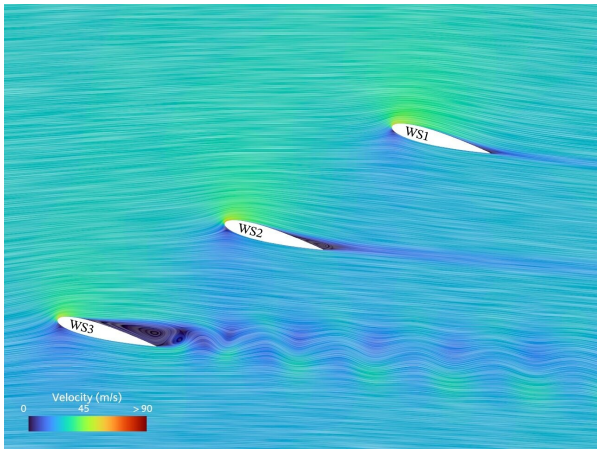

(a) Baseline: 150:15-15-15

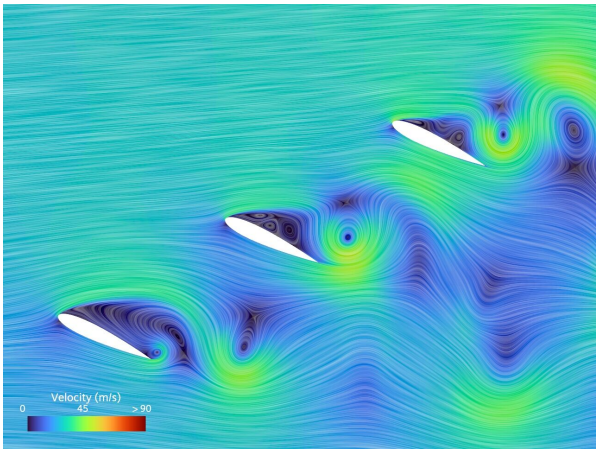

(b) Baseline: 150:25-25-25

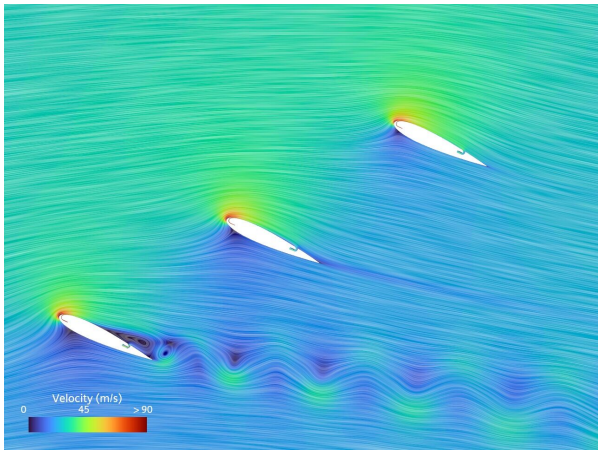

(c) CFJ: 150:25-25-25-CFJ-10-10-10

Figure 4.19: Baseline and CFJ configurations with uniform AoA and C_μ at 150° AWA.

Table 4.7: Coefficient values for baseline at 15° AoA and CFJ at 25° AoA, in a three-sail configuration at 150° AWA.

	WS 1			WS 2			WS 3			Avg.		
	BL	CFJ	Δ	BL	CFJ	Δ	BL	CFJ	Δ	BL	CFJ	Δ
C_L	1.10	2.32	110%	1.06	2.40	126%	0.90	2.08	132%	1.02	2.27	122%
C_D	0.094	0.372	294%	0.043	0.129	198%	0.039	-0.095	-345%	0.059	0.135	130%
C_T	0.63	1.48	134%	0.57	1.31	131%	0.48	0.96	99%	0.56	1.25	123%
C_S	-0.91	-1.82	100%	-0.90	-2.02	124%	-0.76	-1.85	144%	-0.86	-1.90	122%

4.5.3.2 Variable AoA and C_μ at 150° AWA

To optimize the baseline performance at 150° AoA, the AoA is varied for each sail. Reducing the AoA for WS3 to 10° reattaches the flow, as shown in Fig. 4.20a. This results in an increase of C_L for both WS2 and WS3, while WS1 remains largely unaffected. Although C_L for WS3 increases by 7.8%, C_T is reduced by 4.2%. The phenomena of negative drag, first observed on WS1 in the 30:10-15-15 configuration, Fig 4.15, also occurs here for WS3. Once again, it is the sail leading relative to the wind, which in this configuration is WS3. Under broad reach conditions, drag contributes positively to thrust, therefore a reduction in drag leads to a decrease in C_T. This explains the reduction in thrust for WS3, despite its increase in C_L. Further adjustment of WS2, by reducing its AoA by 2°, improves flow attachment, as shown in Fig. 4.20a, but results in a slight decrease in C_T. In terms of C_L and C_D, the 150:15-13-10 configuration offers improved C_L and reduced C_D. However, when evaluated from a ship propulsion perspective, its performance is less favorable. Despite this, achieving a well-attached flow is considered important to avoid any potential oscillations. For this reason, the 150:15-13-10 configurations is selected as the preferred baseline choice for comparison with the CFJ case.

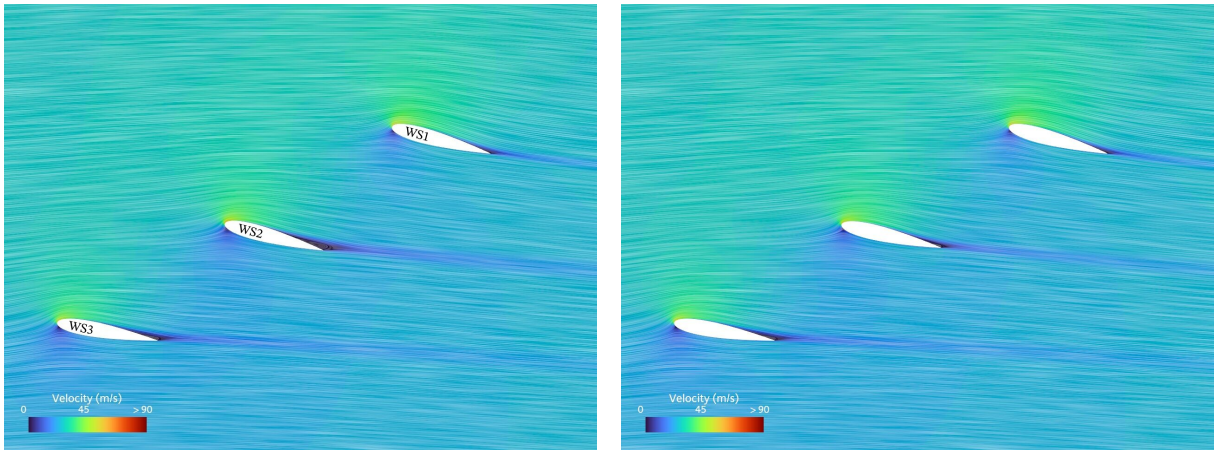

(a) Baseline: 150:15-15-10 (b) Baseline: 150:15-13-10

Figure 4.20: Baseline configurations with variable AoA at 150° AWA.

Table 4.8: Coefficients for baseline configurations with variable AoA at 150° AWA.

	WS	15-15-15	15-15-10	15-13-10
C_L	1	1.10	1.10	1.10
	2	1.06	1.08	1.03
	3	0.90	0.97	0.98
	Avg.	1.02	1.05	1.04
C_D	1	0.094	0.095	0.094
	2	0.043	0.042	0.031
	3	0.039	-0.030	-0.029
	Avg.	0.059	0.036	0.032
C_T	1	0.63	0.63	0.63
	2	0.57	0.58	0.54
	3	0.48	0.46	0.47
	Avg.	0.56	0.56	0.55
C_S	1	-0.91	-0.90	-0.91
	2	-0.90	-0.91	-0.88
	3	-0.76	-0.86	-0.87
	Avg.	-0.86	-0.89	-0.88

Figure 4.21a shows the results of redistributing C_μ to the configuration 25-25-25-CFJ-08-09-13. This redistribution achieves fully attached flow on all three sails without reducing the AoA on WS3, which was necessary in the baseline case. The result is a 2.4% increase in C_T and a 40% reduction in P_c. The well attached flow on WS1 suggests the potential for further increasing its AoA. Increasing the AoA of WS1 to 30° while maintaining the same C_μ distribution leads to improved performance. Although C_L decreases, the increase in C_D contributes to an increase in C_T. As an alternative, maintaining the same AoA for all three sails but altering the C_μ distribution to CFJ-09-09-12 enhances energy efficiency, reducing P_c by 13.6% while keeping C_T unchanged. At an AWA of 150°, fine adjustments of AoA and C_μ have less pronounced impact on thrust compared to the 30° and 90° AWA. This is because both C_L and C_D contribute positively to thrust. The improvement of C_L is associated with the reduction of C_D, which offset each other's contribution to C_T, and changes in one is often offset by changes in the other. However, from the system efficiency perspective, the adjustment of AoA and C_μ is still important to avoid CFJ from operating at separated flow conditions with high P_c. This is evident through comparison of the cases in Figs. 4.21b and c, where C_T is the same but P_c is reduced by 13.6%. The 25-25-25-CFJ-08-09-13 configuration is selected as the preferred design due to its low P_c and only marginal reduction in C_T compared to the case with higher AoA. Comparing the optimal baseline and CFJ configurations 15-13-10 and 30-25-25-CFJ-09-09-12, respectively, the CFJ case achieves a 136% increase in C_T. However, that comes with a 126% increase in C_S.

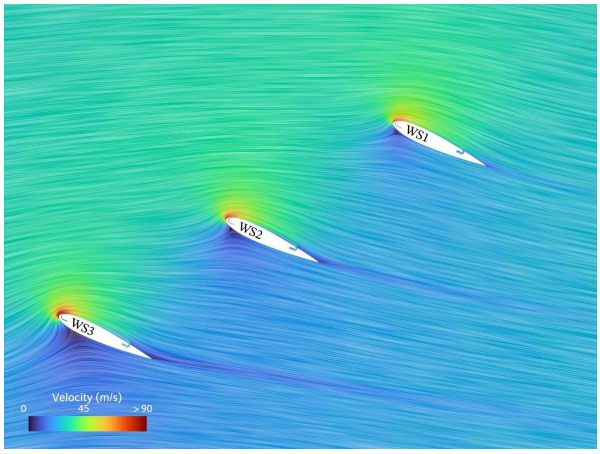

(a) CFJ: 150:25-25-25-CFJ-08-09-13

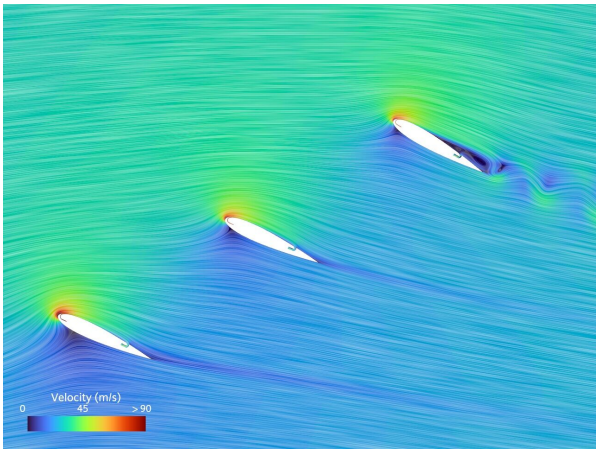

(b) CFJ: 150:30-25-25-CFJ-08-09-13

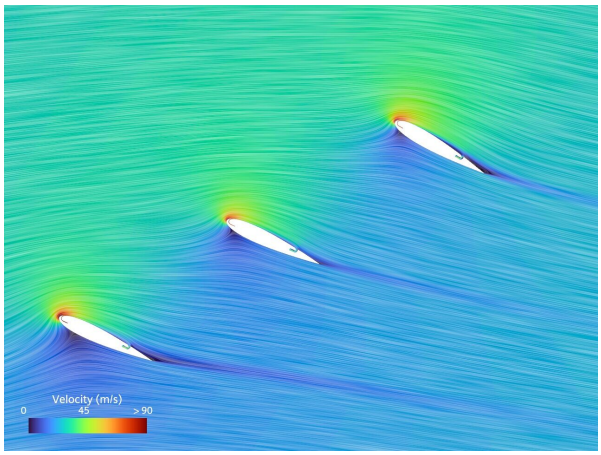

(c) CFJ: 150:30-25-25-CFJ-09-09-12

Figure 4.21: CFJ configurations with variable AoA and C_μ at 150° AWA.

Table 4.9: Coefficients for CFJ configurations with variable AoA and C_μ at 150° AWA.

	WS	25-25-25	25-25-25	30-25-25	30-25-25
C_μ	1	0.10	0.08	0.08	0.09
	2	0.10	0.09	0.09	0.09
	3	0.10	0.13	0.13	0.12
	Avg.	0.10	0.10	0.10	0.10
C_L	1	2.32	2.17	2.08	2.35
	2	2.40	2.28	2.25	2.26
	3	2.08	2.64	2.65	2.51
	Avg.	2.27	2.36	2.33	2.37
C_D	1	0.372	0.359	0.438	0.427
	2	0.129	0.172	0.179	0.156
	3	-0.095	-0.201	-0.159	-0.189
	Avg.	0.135	0.110	0.153	0.131
C_T	1	1.48	1.39	1.42	1.54
	2	1.31	1.29	1.28	1.26
	3	0.96	1.15	1.19	1.09
	Avg.	1.25	1.28	1.30	1.30
C_S	1	-1.82	-1.70	-1.58	-1.82
	2	-2.02	-1.89	-1.86	-1.88
	3	-1.85	-2.39	-2.37	-2.27
	Avg.	-1.90	-1.99	-1.94	-1.99
P_c	1	0.019	0.004	0.026	0.019
	2	0.013	0.009	0.008	0.009
	3	0.043	0.031	0.031	0.029
	Avg.	0.025	0.015	0.022	0.019

5
Conclusion

This thesis has investigated the effects of the CFJ technology applied to a NACA 0015 wingsail. Five parametric studies were carried out, one for the jet momentum coefficient and four for the slot configurations. The resulting CFJ wingsail was adapted to a one-sail study, to investigate the effects on a single wingsail and its net power saving, and a three-sail configuration to study the flow interactions between the sails.

The jet momentum coefficient study reveals that the magnitude of C_μ has a major impact on the performance of the wingsail. All four of the tested cases give an increase in C_L in the entire AoA range. The predominant effect of increasing C_μ is observed in the mid to high AoA region, where each increment raises the maximum C_L and shifts it to a higher AoA. In the low to mid AoA region, the increase in C_L is relatively small, while there is a drastic increase in P_c, resulting in low efficiency. This suggests that for scenarios that demand lower lift, the AoA should be kept low with a low C_μ, while high lift scenarios should use a higher AoA with a higher C_μ. This is supported by the aerodynamic efficiency ($(C_L/C_D)_c$) which is higher for a low C_μ in the low to mid AoA region while it is higher for high C_μ in the mid to high region. The optimal C_μ is therefore dependent on the operating conditions.

For the slot configuration studies, the location and size of the suction slot have little or no impact on C_L. Moving the slot upstream slightly increases P_c while C_L and C_D are kept virtually the same. Its size is of greater importance. While C_L is size independent, decreasing the slot size leads to a large increase in P_c without any performance benefits. However, as the slot size increases, the reduction in P_c eventually diminishes, giving no advantage in increasing it beyond a certain size. The placement of the injection slot affects the P_c to a larger degree than the suction slot. A narrow slot reduces P_c up to an AoA of 25°, with a minimal change in C_L. Moving the slot downstream slightly increases C_L at high AoA, with a marginal delay in stall onset. The decrease in P_c achieved by placing the slot close to the leading edge outweighs any benefit of moving it downstream. The slot design parameter that affects performance the most is the injection slot size. At AoA up to 25° the impact on C_L is small, but the change in P_c is significant, making a wider slot more efficient. For high lift applications, at an AoA of 25° and higher, a narrower slot produces more lift which outweighs the P_c penalty. Based on the parametric study, a CFJ airfoil with design parameters i03-060-s75-200 (injection location at 3%C, injection size of 0.6 %C, suction location at 75%C and suction size of 2%C) offers a good balance between lift and efficiency.

Turning to the one-sail configuration, which compares the CFJ wingsail to a baseline one, the effects of the CFJ technology are evident. The CFJ wingsail increases the C_L by 104% and manages to delay stall onset from 15° to 25° AoA, at the cost of a moderate increase

in C_D. From a fuel consumption perspective, the net power saving is improves over the whole AWA range with a maximum increase of 93% at 90° compared to baseline. In the three-sail configuration, AWA has a major impact on wingsail interactions. Upwash and downwash effects on the leading and trailing wingsails respectively cause flow separation on the leading sail. These effects can be mitigated by adjusting the AoA and C_μ for each wingsail independently. The CFJ enabled wingsails improve the thrust across all tested configurations by between 89% and 123%. These results demonstrate that CFJ is capable of both improving thrust and suppressing flow separation. Combined with its low power consumption, CFJ is a promising technology for fuel savings and reduced emissions.

Bibliography

[1] P. Engström, K. Xu, and R. Bensow, "Performance enhancement of multiple wingsail airfoils using co-flow jet active flow control," in *AIAA SCITECH 2025 Forum*, p. 0485, 2025.

[2] P. Engström, L. Friess, K. Xu, and R. Bensow, "High efficiency co-flow jet wingsail airfoil for sustainable maritime transportation," in *AIAA SCITECH 2026 Forum*, p. 1902, 2026.

[3] United Nations Conference on Trade and Development (UNCTAD), *Review of Maritime Transport 2023: Towards a Green and Just Transition*. United Nations, 2023.

[4] T. Craft, N. Johnson, and B. Launder, "Back to the future? a re-examination of the aerodynamics of flettner-thom rotors for maritime propulsion," *Flow, turbulence and combustion*, vol. 92, pp. 413–427, 2014.

[5] R. Lu and J. W. Ringsberg, "Ship energy performance study of three wind-assisted ship propulsion technologies including a parametric study of the flettner rotor technology," *Ships and Offshore Structures*, vol. 15, no. 3, pp. 249–258, 2020.

[6] M. Traut, P. Gilbert, C. Walsh, A. Bows, A. Filippone, P. Stansby, and R. Wood, "Propulsive power contribution of a kite and a flettner rotor on selected shipping routes," *Applied energy*, vol. 113, pp. 362–372, 2014.

[7] G. Rutkowski, "Study of green shipping technologies-harnessing wind, waves and solar power in new generation marine propulsion systems," *TransNav: International Journal on Marine Navigation and Safety of Sea Transportation*, vol. 10, no. 4, pp. 627–632, 2016.

[8] A. Kukner, S. Bulut, and A. N. Halilbese, "Renewable energy options and an assessment of wind-based propulsion systems for small crafts," *Naval Academy Scientific Bulletin. http://dx. doi. org/10.21279/1454-864X-16-I2-006*, 2016.

[9] G. M. Dadd, D. A. Hudson, and R. Shenoi, "Determination of kite forces using three-dimensional flight trajectories for ship propulsion," *Renewable Energy*, vol. 36, no. 10, pp. 2667–2678, 2011.

[10] K. Malmek, L. Larsson, S. Werner, J. W. Ringsberg, R. Bensow, and C. Finnsgård, "Rapid aerodynamic method for predicting the performance of interacting wing sails," *Ocean Engineering*, vol. 293, p. 116596, 2024.

[11] H. Zhu, H.-D. Yao, F. Thies, J. W. Ringsberg, and B. Ramne, "Propulsive performance of a rigid wingsail with crescent-shaped profiles," *Ocean Engineering*, vol. 285, p. 115349, 2023.

[12] J. Cairns, M. Vezza, R. Green, and D. MacVicar, "Numerical optimisation of a ship wind-assisted propulsion system using blowing and suction over a range of wind conditions," *Ocean Engineering*, vol. 240, p. 109903, 2021.

[13] H. Lee, Y. Jo, D.-J. Lee, and S. Choi, "Surrogate model based design optimization of multiple wing sails considering flow interaction effect," *Ocean Engineering*, vol. 121, pp. 422–436, 2016.

[14] I. M. Viola, M. Sacher, J. Xu, and F. Wang, "A numerical method for the design of ships with wind-assisted propulsion," *Ocean Engineering*, vol. 105, pp. 33–42, 2015.

[15] E. Blackert, U. Dhomé, A. Hillenbrand, C. Fagergren, J. Kuttenkeuler, and F. Gerhardt, "Wind tunnel tests of a wind-powered car carrier," in *The 8th International Conference on Advanced Model Measurement Technology for the Maritime Industry*, KRISO (Korea Research Institute of Ships & Ocean Engineering), 2025.

[16] G. Zha, W. Gao, and C.D. Paxton, "Jet Effects on Co-Flow Jet Airfoil Performance," *AIAA Journal*, vol. 45, pp. 1222–1231, 2007.

[17] K. Xu and G. Zha, "Investigation of coflow jet active flow control for wind turbine airfoil," in *AIAA aviation 2020 forum*, p. 2942, 2020.

[18] K. Xu and G. Zha, "Design of high specific speed mixed flow micro-compressor for co-flow jet actuators," in *Turbo Expo: Power for Land, Sea, and Air*, vol. 58714, p. V008T26A014, American Society of Mechanical Engineers, 2019.

[19] K. Xu and G. Zha, "Improving efficiency of co-flow jet micro-compressor actuator outlet guide vanes and nozzle," in *AIAA Aviation 2019 Forum*, p. 3495, 2019.

[20] P. A. Barrios, Y. Ren, K. Xu, and G. Zha, "Design of 3d co-flow jet airfoil with integrated micro-compressor for high operating efficiency at cruise condition," in *AIAA AVIATION 2021 FORUM*, p. 2581, 2021.

[21] K. Xu and G. Zha, "Study of axial groove casing treatment for co-flow jet micro-compressor actuators," in *AIAA Scitech 2021 Forum*, p. 1560, 2021.

[22] D. Kaklis, P. Eirinakis, G. Giannakopoulos, C. Spyropoulos, T. J. Varelas, and I. Varlamis, "A big data approach for fuel oil consumption estimation in the maritime industry," in *2022 IEEE Eighth International Conference on Big Data Computing Service and Applications (BigDataService)*, pp. 39–47, IEEE, 2022.

[23] M. Tadros, M. Ventura, and C. Guedes Soares, "Review of the decision support methods used in optimizing ship hulls towards improving energy efficiency," *Journal of Marine Science and Engineering*, vol. 11, no. 4, p. 835, 2023.

[24] Royal Academy of Engineering, "Future ship powering options: exploring alternative methods of ship propulsion," 2013.

[25] M. Gad-el-Hak, *Flow Control: Passive, Active, and Reactive Flow Management*. Cambridge, UK: Cambridge University Press, 2000.

[26] T. Ogawa, K. Asada, M. Sato, T. Tatsukawa, and K. Fujii, "Computational study of the plasma actuator flow control for an airfoil at pre-stall angles of attack," *Applied Sciences*, vol. 12, no. 18, p. 9073, 2022.

[27] J. Wang and L. Feng, *Flow control techniques and applications*. Cambridge University Press Cambridge, UK, 2019.

[28] G.-C. Zha and C. Paxton, "A Novel Airfoil Circulation Augment Flow Control Method Using Co-Flow Jet." NASA/CP-2005-213509, June 2005; AIAA Paper 2004-2208, June 2004.

[29] F. Menter, "Zonal Two Equation $k-\omega$ Turbulence Models for Aerodynamic Flows." AIAA Paper 93-2906, 1993.

[30] L. S. Caretto, A. Gosman, S. V. Patankar, and D. Spalding, "Two calculation procedures for steady, three-dimensional flows with recirculation," in *Proceedings of the Third International Conference on Numerical Methods in Fluid Mechanics: Vol. II Problems of Fluid Mechanics*, pp. 60–68, Springer, 2007.

[31] G.-C. Zha, W. Gao, and C. Paxton, "Jet Effects on Co-Flow Jet Airfoil Performance," *AIAA Journal, No. 6,*, vol. 45, pp. 1222–1231, 2007.

[32] R. E. Sheldahl and P. C. Klimas, "Aerodynamic characteristics of seven symmetrical airfoil sections through 180-degree angle of attack for use in aerodynamic analysis of vertical axis wind turbines," tech. rep., Sandia National Lab.(SNL-NM), Albuquerque, NM (United States), 1981.

[33] F. Bertagnolio, "Naca0015 measurements in lm wind tunnel and turbulence generated noise," 2008.

[34] A. Christian, S. Tobing, and R. Kurniawan, "A numerical analysis on the effects of angle-of-attack and stagger on the propulsion of tandem airfoil at high and low speed flight,"

CHALMERS UNIVERSITY OF TECHNOLOGY
Gothenburg, Sweden
www.chalmers.se

CHALMERS
UNIVERSITY OF TECHNOLOGY